Light absorption and morphological properties of soot-containing aerosols observed at an East Asian outflow site, Noto Peninsula, Japan

S. Ueda[1,2], T. Nakayama[1,3], F. Taketani[4], K. Adachi[5], A. Matsuki[6], Y. Iwamoto[6,7], Y. Sadanaga[8] and Y. Matsumi[1,3]

[1]{Solar-Terrestrial Environment Laboratory, Nagoya University, Nagoya, Japan}

[2] {Now at Graduate School of Environmental Studies, Nagoya University, Nagoya, Japan}

[3] {Now at Institute for Space-Earth Environmental Research, Nagoya University, Nagoya, Japan}

[4]{Japan Agency for Marine-Earth Science and Technology, Yokohama, Japan}

[5]{Atmospheric Environment and Applied Meteorology Research Department, Meteorological Research Institute, Tsukuba, Japan}

[6]{Institute of Nature and Environmental Technology, Kanazawa University, Kanazawa, Japan}

[7]{Now at Faculty of Science Division I, Tokyo University of Science, Tokyo, Japan}

[8]{Graduate School of Engineering, Osaka Prefecture University, Osaka, Japan}

Correspondence to: S. Ueda (ueda-s@stelab.nagoya-u.ac.jp) and T. Nakayama (nakayama@stelab.nagoya-u.ac.jp)

Abstract

The coating of black carbon (BC) with inorganic salts and organic compounds can enhance the magnitude of light absorption by BC. To elucidate the enhancement of light absorption of aged BC particles and its relation to the mixing state and morphology of individual particles, we conducted observations of particles at an Asian outflow site in Noto Peninsula, Japan, in the spring of 2013. Absorption and scattering coefficients at 405, 532, and 781 nm and mass concentrations/mixing states of refractory-BC in PM2.5 were measured using a three-wavelength photoacoustic soot spectrometer and a single-particle soot photometer

(SP2), respectively, after passage through a thermodenuder (TD) maintained at 300 °C or 400 °C or a bypass line maintained at room temperature (25 °C). The average enhancement factor of BC light absorption due to coating was estimated by comparing absorption coefficients at 781 nm for particles that with and without passing through the TD at 300 °C and was found to be 1.22. The largest enhancements (>1.30) were observed under high absorption coefficient periods when the air mass was long-range transported from urban areas in China. Aerosol samples were also analyzed using a transmission electron microscope (TEM) equipped with an energy dispersive X-ray analyzer. The morphological features and mixing states of soot-containing particles of four samples collected during the high absorption events were analyzed by comparing microphotographs before and after the evaporation of beam-sensitive materials by irradiation with a high density electron beam. The majority of the soot in all samples was found as mixed particles with sulfate-containing spherules or as clusters of such spherules. For samples showing high enhancement (>1.30) of BC light absorption, TEM showed that the internally mixed soot-containing particles tended to have a more spherical shape and to be thickly-coated. The SP2 measurements also suggested that the proportion of thickly-coated soot was greater. Thus, the observed enhancement of BC light absorption was found to differ according to the mixing states and morphology of soot-containing particles. The enhancement of BC light absorption in our *in situ* measurements and its relation with individual features of soot-containing particles will be useful to evaluate direct radiative forcing in the downwind areas of large emission sources of BC.

1 Introduction

Black carbon (BC) is contained in particles emitted from fossil fuel combustion and biomass/biofuel burning. It is known as a strong absorber of visible spectrum solar radiation in the atmosphere (e.g., Ramanathan and Carmichael, 2008; Bond et al., 2013). Similar to greenhouse gases, this absorption by BC is thought to lead to large positive radiative forcing; however, this assumption remains uncertain (IPCC, 2013). In the estimation of direct radiative forcing by BC particles, understanding how to treat the mixing state and optical properties of the BC and other materials are particularly important factors for reducing this uncertainty (Ma et al., 2012). In relation to the global effect of BC, marked anthropogenic emissions of pollutants by recent economic development in eastern Asia is an important

consideration (Streets et al., 2003; Ohara et al., 2007; Kurokawa et al., 2013). In addition to BC, precursor gases of secondary aerosol materials have been heavily emitted in eastern Asia (Bond et al., 2004; Kurokawa et al., 2013).

BC is operationally defined as a carbonaceous material with a deep black appearance caused by a significant imaginary portion of the refractive index. It roughly corresponds with elemental carbon (EC), which refers to the nonvolatile carbon present below a certain temperature (typically 550 °C) (Andreae and Gelencsér 2006, Bond and Bergstrom, 2006). Carbonaceous particles originating from fossil fuel combustion are observed as soot by electron microscope (e.g., Murr and Soto, 2005). Soot has an aggregation morphology of globules with a diameter of tens of nanometres that consist of concentrically wrapped graphitic layers (Pósfai et al., 2004; Murr and Soto, 2005). Although the definitions of soot and BC are different, they were considered equivalent for the purposes of this work. Soot particles that are freshly emitted by fossil fuel combustion are attached/coated with secondary aerosol materials, such as sulfate, nitrate, and organics, through atmospheric aging processes (Weingartner et al., 1997; Zuberi et al., 2005). Atmospheric aging processes of aerosol particles include adsorption and condensation of semi-volatile materials, coagulation of particles with other pre-existing aerosol particles, heterogeneous reactions at the particle surface with gaseous species, and cloud processing in the atmosphere (Fuchs, 1964; Husar and Whitby, 1973; Mamane and Gottlieb, 1989; Meng and Seinfeld, 1994; Ueda et al., 2014). Several studies using electron microscopy have reported that soot particles tend to be coated with large amounts of secondary materials in an aged air mass, whereas air masses in urban areas contain some uncoated soot particles (Pósfai et al., 1999; Hasegawa et al., 2002; Vester et al., 2007; Ueda et al., 2011; Adachi et al., 2014). Ueda et al. (2011) reported that in leeward areas, soot-containing particles were internally mixed with the largely soluble materials in polluted air masses transported from eastern Asia. Moreover, a fraction of the soot-containing particles had an irregular shape due to mixing with clusters of spherical sulfate, that is, considered to be generated by coagulation processes under dry and high aerosol concentration conditions.

The presence of coatings on BC particles is known to enhance the magnitude of light absorption by the BC particles, referred to as the “lensing effect”. The enhancement of light absorption by BC particles by coating (E_{abs}) is expressed as the ratio of light absorption of coated BC particles to uncoated BC particles. Models often apply a constant E_{abs} value or

estimate E_{abs} assuming a core-shell (the BC core and coating materials) shaped spherical particle (Bond et al., 2013 and references therein). However, several studies have indicated that estimation assuming a core-shell structure with a clear shell tends to overestimate the E_{abs} values (Lack and Cappa, 2010; Adachi et al., 2010). Lack and Cappa (2010) estimated E_{abs} of BC particles coated by brown carbon based on calculations using core-shell Mie theory. They showed that the lensing effect can be reduced from the non-absorbing coating case by up to 25%–30% when averaged across the visible radiation spectrum. For Mexico City, Adachi et al. (2010) obtained three-dimensional shapes of soot-containing particles embedded in organic matter and sulfate using electron tomography with a transmission electron microscope (TEM), and calculated the optical properties using a discrete dipole approximation. They reported that the core-shell model overestimated light absorption by ~30% compared to the model for irregularly shaped soot-containing particles.

Recently, the E_{abs} values have been measured by several studies based on *in situ* measurement of optical properties, using photoacoustic spectrometers (PAS) with a thermodenuder (TD). The reported E_{abs} values are from non-detectable to 1.43 in Toronto (Canada) (Knox et al., 2009, Chan et al., 2011, Healy et al., 2015), 1.38 in Boulder (USA) (Lack et al., 2012), 1.06 in California (USA) (Cappa et al., 2012), 1.10 (August) and non-detectable (January) in Nagoya (Japan) (Nakayama et al., 2014), and 1.4 at Detling (UK) (Liu et al., 2015). In these studies, E_{abs} was estimated as the ratio between absorption of ambient particles and particles heated in a TD to remove non-BC materials. However, there have been very few observational studies reported the contributions of lensing effect and their relation with morphology of individual BC-containing particles in a well-aged air mass.

To elucidate the enhancement of light absorption of aged BC particles of Asian outflow and their relation with the amount, morphology, and composition of coating materials, we conducted atmospheric observations of continental outflow at Noto Peninsula, Japan, in spring 2013. This atmospheric observation site has been previously used to study continental outflow (Maki et al., 2010; Iseki et al., 2010; Ishiyama et al., 2015). In the present study, the absorption and scattering coefficients of aerosol particles were directly measured using a 3λ-photoacoustic spectrometer (Droplet Measurement Technologies, PASS-3) with and without passage through a TD, and the contribution of the lensing effect was estimated. Specific attention was given to the relations between the enhancement of light absorption and the coating condition of individual soot-containing particles based on the TEM analysis.

2 Field observation and laboratory analysis methods

2.1 Observation site and instrumentation

Atmospheric observations were conducted at NOTO Ground-based Research Observatory (NOTOGRO) in Suzu City, Japan (37.5 °N, 137.4 °E), from April 17 to May 14, 2013. Suzu City is located on the north coast of Noto Peninsula. The physical and chemical parameters of aerosol particles and the concentrations of gaseous species have been continually monitored at the site. Ambient air was sampled through a PM10 inlet that was placed 14.7 m above the ground. Each measurement system was set in a room and connected to a flow-splitter downstream of the PM10 inlet. Chemical constituents of the aerosols were assessed using an aerosol chemical speciation monitor (Aerodyne Research, ACSM) capable of monitoring the bulk chemical components (organics, NH_4^+, SO_4^{2-}, NO_3^-, and Cl^-) of non-refractory submicrometer-sized aerosols (NR-PM_1). A $PM_{2.5}$ cyclone (with a cut off size of 2.5 μm at a flow rate of 3 L min^{-1}) was installed upstream of the ACSM inlet to remove coarse particles. The ionization efficiency of nitrate and the relative ionization efficiency of ammonium were determined by the standard calibration procedure (Ng et al., 2011) using NH_4NO_3 (99.5%, Strem Chemicals). A collection efficiency (CE) of 0.3 was applied to the ACSM data. The value of CE was determined by comparing the mass concentrations of ammonium and sulfate derived by the ACSM to those measured by a conventional filter based off-line chemical analysis. The procedures to determine the CE value are described in the Supplemental Material (S1). It should be noted that selection of the CE value itself does not affect the discussion in this study, although the uncertainties in mass concentrations of NR components may be large (see section S1). Data for the chemical constituents were obtained every 30 min. During our observation period, more than 90% of the measured non-refractory materials were SO_4^{2-}, NH_4^+, and organics by mass. A particle size distribution between 8 and 346 nm in diameter was measured by a scanning mobility particle sizer (SMPS) (TSI, model 3936L76) placed downstream of the PM10 inlet. We set additional systems in the flow-splitter downstream of the PM10 inlet during this observation campaign, as shown in sections 2.2 and 2.3.

The concentrations of NO_x and NO_y were measured using a NO–O_3 chemiluminescence detector (Thermo Fisher Scientific, model 42i-TL) with a near-UV LED photolytic converter

and a molybdenum reduction catalyst (Mo converter) (Thermo Fisher Scientific, part No. 9445) heated to 598 K, respectively. Detailed information for these measurements of NO_x (Sadanaga et al., 2010) and NO_y (Sadanaga et al., 2008; Yuba et al., 2010; 2014) have been given previously.

2.2 *In situ* measurements of optical and physical properties of particles with and without passage through the TD

A schematic diagram of the experimental setup to measure the optical and physical properties of particles with or without passage through a TD is presented in Figure 1. Coarse aerosol particles were removed by a $PM_{2.5}$ cyclone (URG, URG-2000-30EH). After being dried by diffusion dryers with silica gel, the sample air was introduced alternately to a reference line and two TD lines to measure, respectively, ambient particles directly and after the evaporation of volatile materials under high temperature conditions. The same type of TDs used in our previous studies (Guo et al., 2014; Nakayama et al., 2014) was used in this study. The TD consists of a stainless tube (outer and inner diameters: 12.7and 10.2 mm, respectively; length: 600 mm) and electronic jacket heaters (Heater Engineer, P-series). Flow rates through the TD was 1.28 lpm, and the residence time for the sample aerosols in the TD was estimated to be 2.3 s, on the assumption of plug flow conditions (at 20°C). The temperatures of the two TDs were maintained at 300 °C and 400 °C. The lines were switched every 10 min using two-way ball valves. Then, the sample air was introduced to the PASS-3, another SMPS (TSI, model 3936L72), and a single-particle soot photometer (Droplet Measurement Technologies, SP2). The sampling flow rates of the PASS-3, SMPS, and SP2 were 1.0, 0.2, and 0.08 L min^{-1}, respectively. The relative humidity in the cell of the PASS-3 was lower than 11% throughout the observation period.

The SMPS was used to measure the particle size distribution between 18 and 982 nm in diameter every 5 min. The SP2 was used to measure the mass concentration, size, and mixing state of single refractory BC (rBC) particles. The SP2 is based on the laser-induced incandescence (LII) method. The basic measurement principle of SP2 has been described previously (Gao et al., 2007; Moteki and Kondo, 2007). Before and after measurement, calibration of rBC was performed by measuring the LII signal intensities from size-specified fullerene particles (Alfa Aesar; stock 40971, lot L20W054) generated by an atomizer through

a differential mobility analyzer (DMA) (TSI, model 3080). The size of rBC was derived by assuming sphericity and a fixed density of 1.8 g/cm^3. The mixing state of rBC-containing particles was qualitatively estimated by the lag-time of the LII peak with respect to the peak of the scattering signal (Moteki and Kondo, 2007). Use of the SMPS in our measurement system was ended on 13 May, while use of the PASS-3 and SP2 was ended on 14 May.

The PASS-3 instrument was used to measure the absorption [$b_{abs}(\lambda)$] and scattering [$b_{sca}(\lambda)$] coefficients at 405, 532, and 781 nm. Details of the performance and calibration procedures of the PASS-3 have been described elsewhere (Nakayama et al., 2013, 2015). Note that the absolute values of the calibration factors do not influence to the E_{abs} values, which are used for discussion in the present study. The b_{sca}(532 nm) data were not used in this study because of a strong particle size dependence of the calibration factor at 532 nm (Nakayama et al., 2015). For background interpolation, measurements of filtered air were conducted using a particulate filter (Balston) for 3 min every 10 min. The influence of light absorption of NO_2 was found to be small (<0.05 and <0.04 Mm^{-1} at 405 and 532 nm, respectively) based on the estimation using transmittance of NO_2 through filter and inlet tube as well as mixing ratio of NO_2, and was taken into account for the determination of b_{abs} values. The 3-hour averaged values for each sampling line were estimated from six sets of 10 min data. By taking two standard deviations (2σ) of each signal during the filtered air measurements, the typical detection limits for the 3-hour averaged data of b_{abs} (405 nm), b_{abs} (532 nm), b_{abs} (781 nm), b_{sca} (405 nm), and b_{sca} (781 nm) were estimated to be 1.0, 1.9, 1.1, 0.7, and 0.3 Mm^{-1}, respectively. Note that these detection limits varied depending on the magnitude of the drift in each signal.

In our system, particle loss and charring can occur in the TD lines. Using thermal/optical methods, some analytical studies of elemental and organic carbon in atmospheric particles reported that the degree of increase in light absorption of particles by charring differed among different organic material compositions (Yang and Yu, 2002; Yu et al., 2002). Based on the measurement of absorption at 680 nm wavelength under He induced conditions, Yang and Yu (2002) showed that charring of a sample including a large amount of water soluble organic carbon can increase from around 400 °C. The charring effect can vary depending on the aerosol composition and, therefore, with time. In this observation, the ratios of the mass concentration of rBC measured by the SP2 without heating [m_{rBC}(25 °C)] to that after heating [$m_{rBC}(T)$] (T = 300 and 400°C) varied depending on time with averages (± 1σ) of 1.08 ± 0.28

and 1.03 ± 0.30 at 300 °C and 400 °C, respectively. Considering the estimated particle loss in our TD (~17% and ~20% at 300 and 400 °C, respectively (Guo et al. 2014)), our results suggest that non-negligible amount of rBC (10%–20% of ambient rBC) were formed in the TD, possibly due to charring by heating. In the present study, the E_{abs} values were estimated by taken these effects into account, assuming that light absorbing property of ambient rBC is same with that of rBC formed by hearting in the TD and detected by the SP2,

$$E_{\mathrm{abs}}(\lambda,\ T)\ = \frac{b_{\mathrm{abs}}(\lambda,25\ ^{\circ}\mathrm{C})/b_{\mathrm{abs}}(\lambda,T)}{m_{\mathrm{rBC}}(25\ ^{\circ}\mathrm{C})/m_{\mathrm{rBC}}(T)}, \quad (1)$$

where λ and T were measurement wavelength and TD temperature, respectively.

2.3 Samples of individual particles and TEM analyses

Aerosol particles were collected for morphological analysis using TEM (JEM-1400; JEOL). The sampling line for TEM analysis was placed downstream of the PM10 inlet. To analyze particles under the same conditions as PASS-3 and SP2, dried aerosols (after passage through diffusion dryers) were collected using a two-stage cascade impactor (50% cutoff aerodynamic diameters of the two stages were 1.5 μm and 0.3 μm at a flow rate of 0.7 L min^{-1}) on carbon-coated nitrocellulose (collodion) films. In this study, samples from the second stage (50% cut off diameter of 0.3 μm) were analyzed. Aerosol samples were collected for 10–20 min. Typically, 1–2 samples were taken per day during the campaign. A fraction of the samples was collected after passing the particles through the same type of TDs used for the *in situ* measurements (section 2.2) maintained at 300 or 400 °C. The TEM samples were stored under dry conditions at room temperature until analyses. According to the b_{abs} values, the four samples obtained without passing the particles through the TD and one sample obtained after passing the particles through the TD maintained at 400 °C were selected and analyzed.

To obtain stereoscopic information of particles from 2-dimensional microphotograph, particles were coated with a Pt/Pd alloy at a shadowing angle of 26.6° (arctan 0.5), according to the method of Okada (1983). The Pt/Pd coating thickness was about 7 Å. The scanned image was processed using image analysis software (Win Roof; Mitani Corp.) to estimate the projected area of the particles. Elemental compositions of individual particles were analyzed using an energy-dispersive X-ray spectrometer (EDS) along with the TEM. The EDS was operated at an accelerating voltage of 120 kV. Elemental analyses were performed for C, Na, Mg, Al, Si, P, S, Cl, K, Ca, Ti, V, Cr, Mn, Fe, Ni, Zn, Sn, and Pb. The X-ray spectrum was

obtained using a detector with a counting time of 20 s per particle. The peak intensities of the elemental compositions in individual particles were quantified from the spectrum after deduction of the background spectrum near the particles. Based on the peak intensity, compositional particle types were classified as sulfate-rich, carbon-rich, sea salt-rich, aged sea salt-rich, crustal-rich, or others. Carbon-rich particles have the largest C peak. Sulfate-rich particles have the largest S peak and are absent of Na. Sea salt-rich particles have the largest Na peak or are Na-containing particles having the largest Cl peak. Aged sea salt-rich particles are Na-containing particles having the largest S peak. Crustal-rich particles have the largest peaks of Al, Si, or Fe. Particles having peaks other than those above, or not having a detectable peak, were classified as others. In this classification, a spectrum larger than two times the standard deviation of the background spectra, which are spectra for non-particle areas measured between each sample analysis, was used as the detectable spectrum of the particles to eliminate background noise effects. However, it should be noted that the standard deviation of the background C spectra is high because of the use of C-coated collodion film; therefore, there is a possibility that the number of C-rich particles is actually higher than that counted. To overcome this, the ratio of C to another element before elimination of the noise was utilized as an index of carbon content (Section 3.3.2).

3 Results and discussion

3.1 Temporal variation of optical properties

Figure 2 shows the temporal variations in absorption [$b_{abs}(\lambda)$] and scattering [$b_{sca}(\lambda)$] coefficients and enhancement of light absorptions [$E_{abs}(\lambda)$] observed during April 17–May 14, 2013. Averages of $b_{abs}(\lambda)$ and $b_{sca}(\lambda)$ during the entire observation period are listed in Table 1. The b_{abs}(405 nm) and b_{abs}(781 nm) at 25 °C varied from close to 0 to 10 Mm^{-1} and 0 to 5 Mm^{-1}, respectively. High $b_{abs}(\lambda)$ events (higher than 5 Mm^{-1} at 405 nm) were observed on April 19, 22, and 27–29 and on May 6, 10, and 13–14. The b_{sca} at 25 °C was almost synchronous with b_{abs}, but the values were about ten times larger (Table 1). For sample air that passed through the TD at 300 °C and 400 °C, averaged b_{sca} values were, respectively, one-seventh and one-eighth of those at 25 °C at 405 nm, and one-fourth of those at 25 °C at 781 nm (Figure 2b and d). In contrast, the values of b_{abs}(405 nm) and b_{abs}(781 nm) at high temperature (300 °C and 400 °C) were only slightly different from those at 25 °C (Figure 2a and c).

Most of the E_{abs}(405 nm) values on April 19, 22–23, 26–29, and May 5–6 were less than 1.0 and also less than the E_{abs}(532 nm) and E_{abs}(781 nm) values, while the $E_{abs}(\lambda)$ values on May 13–14 were greater than 1.0 at all wavelengths. Averaged $E_{abs}(\lambda)$ for the data above the detection limit during the entire observation period are also listed in Table 1. Similar averaged $E_{abs}(\lambda)$ values between 300 °C and 400 °C were obtained at each wavelength. Because brown carbon is considered to absorb light only at shorter visible and UV wavelengths (Andreae and Gelencsér, 2006; Moosmüller et al., 2009), E_{abs}(405 nm) was expected to be larger than E_{abs}(781 nm) if light absorption by organic materials evaporated at temperatures below 300 or 400 °C contributed to the total light absorption at 405 nm. However, this study produced the opposite result. This can be explained by the increase of ″brownish materials″ by heating. Here, the ″brownish materials″ are defined as the materials which were generated by heating in the TD and had significant light absorption at shorter visible wavelengths, to distinguish with ambient brown carbon particles.

In this study, as explained in the previous section, $b_{abs}(\lambda)$ was corrected for the effect of loss and formation of rBC inside the TDs using the mass concentration of rBC measured by SP2. However, the absorption by brownish materials that was potentially formed in the TDs might not be corrected accurately using this method because of the difference in wavelength dependence of light absorption between BC and brownish materials. According to the above explanation, E_{abs}(405 nm) and E_{abs}(532 nm) might have been particularly underestimated due to the absorption by brownish materials formed in the TDs. Because the influence of the formation of brownish materials on E_{abs}(781 nm) should be minimal, E_{abs}(781 nm) is considered to represent the lensing effect in later discussions.

It should be noted that E_{abs}(781 nm) was calculated using eq (1) on the assumption that the light absorbing property of ambient rBC was same with that of rBC generated in the TD. If mass absorption cross section at 781 nm for rBC generated in the TD would be different by 50% with that for ambient rBC, the lensing effect could be underestimated or overestimated by 0.05–0.10, considering 10%–20% of rBC were generated by heating in the TD (section 2.2).

3.2 Relations between backward air mass trajectories and optical properties

Figure 3 presents (a) the location of NOTOGRO, and (b-e) the 3 day backward air trajectories for air masses reaching the observation site. The backward trajectory data were computed

using the Hybrid Single-Particle Lagrangian Integrated Trajectory (HYSPLIT 4) model developed by the National Oceanic and Atmospheric Administration (NOAA) Air Resources Laboratory (ARL) (Draxler and Rolph, 2003; Rolph, 2003). The trajectories are colored according to b_{abs} (405 nm) and b_{abs} (781 nm), and to E_{abs}(405 nm) and E_{abs}(781 nm) calculated from b_{abs} values at 25 °C and 300 °C. The trajectories for E_{abs} calculated from b_{abs} data below the detection limit are presented as thin lines in Figures 3d and e.

The b_{abs} tended to be greater in air masses from the East Asian continent and lower in air masses from the north, such as from the Okhotsk Sea. When the greatest b_{abs} value was observed on the morning of May 14, the air mass originated from around Shanghai and was transported over the East China Sea. Large amounts of BC and precursors of secondary aerosols are considered to be emitted from the industrial areas facing the Yellow Sea and East China Sea in eastern China (Streets et al., 2003; Bond et al., 2004). Pollution events involving large amount of aerosols have been reported around the industrial areas in eastern China (Gao et al., 2009) and their leeward areas (Takami et al., 2005, 2007).

The E_{abs} at both 405 and 781 nm tended to differ according to the origin of the air mass: the E_{abs} was high (1.3–1.4 at 405 nm and 1.3–1.5 at 781 nm) when air mass originated from around Shanghai and was transported over the East China Sea (May 13–14), and was low (< 1.0 at 405 nm and 1.0–1.3 at 781 nm) when the air mass originated from northern China or Siberia and was transported over northern Korea peninsula and the sea of Japan (April 19, 22, 27, and 28), or from the sea of Japan or a region of the main island of Japan (April 22 and 29 and May 6 and 10). The E_{abs} values for the air mass from the Okhotsk Sea were not determined because the absorption coefficients were below the detection limit.

3.3 TEM analyses

3.3.1 Physicochemical properties of aerosols

The four samples collected during high b_{abs} events in May were analyzed using TEM. The start times of the sampling are shown with the arrows A–D in Figure 2a. The details of the samples are listed in Table 2. For all samples, the average E_{abs}(405 nm) values were smaller than the average E_{abs}(781 nm) values by 0.1–0.4.

Ratio of NO_x to NO_y has been used as an indicator of photochemical age of air mass (e.g., Cappa et al., 2012). The ratio for samples A, B, C, and D were 0.43, 0.67, 0.38, and 0.24, respectively. The results suggest that the plume ages for samples C and D are greater than those for samples A and B, although quantitative estimation of the plume age is difficult due to the possible contributions of wet and dry depositions of NO_y.

Figure 4 portrays the 72-hour horizontal backward trajectories of air parcels for samples A, B, C, and D, starting at 500 m above sea level at the NOTOGRO site. The trajectories for samples A and B showed that the air masses were transported slowly and reached the observation site over the north coast of the main island of Japan. The air masses for sample C were from northern China and were transported over the Korean Peninsula and the Sea of Japan, while those for sample D were from the Shanghai area and were transported over the East China Sea and the Sea of Japan within ~3 days. Combining these trajectories with the results of the ratios of NO_x to NO_y, indicates that samples A and B were likely affected by emissions from the main island of Japan, while samples C and D could be considered to be mainly affected by continental outflow.

For samples A, B, and D, 96%, 88%, and 97%, respectively, of the mass concentration of non-refractory materials measured by the ACSM consisted of SO_4^{2-}, NH_4^+, and organics (Table 2). The organic mass ratio for samples A, B, and D were 62%, 62%, and 24%, respectively. The BC mass concentrations measured by SP2 were 4%, 3%, and 2% of the total submicron particle mass (sum of the mass concentrations of BC and non-refractory materials) for samples A, B, and D, respectively. The inlet line of the ACSM system was connected to a different line from 12:00 May 12 to 17:30 May 13, 2013, and the data for this period are not used in this study.

Figure 5 presents number–based size distributions at 25 °C, 300 °C, and 400 °C, and the cross sectional area- and volume-based size distributions at 25 °C of aerosol particles during samplings A–D, as measured by SMPS. Because use of the SMPS (TSI, model 3696L72) placed downstream of the heating system (shown in Figure 1) was ended on May 13, the 8–346 nm size distribution measured by another SMPS (TSI, model 3936L76) placed downstream of the PM10 inlet is used on May 14. Number-size distribution at 25 °C shows that number concentrations were higher in the < 100 nm fraction for samples A and B, but for samples C and D were higher in the > 100 nm fraction. The inlet line of the ACSM system was connected to a different line from 12:00 May 12 to 17:30 May 13, 2013, and the data for

this period are not used in this study. By passing the particle through the TD maintained at 300 °C or 400 °C, the total particle number concentration decreased by one-fourth to one-half and the distribution had peaks in the < 100 nm fraction for samples A–C. In contrast, particles with diameters between 100 to 400 nm mainly contributed to the total cross-sectional area and volume of particles for all samples, and this is considered to contribute mainly to their optical properties.

Figure 6a presents the mass equivalent size distributions of rBC measured by SP2 for samples A–D together with their log-normal best-fitting curves. The peak diameters were around 200 nm for all samples and were slightly larger for samples C and D compared to those for samples A and B. Figure 6b presents the normalized-count distribution of lag-time for rBC with a mass equivalent diameter of 200 ± 10 nm. Unfortunately, the coating thickness of rBC could not be obtained directly by SP2 in this study because of a mechanical issue on a detector to determine absolute position of particles in the laser beam. Instead, the lag-time is treated as an index of the mixing states of rBC-containing particles because the scattering signal of the thicker-coated rBC core is detected before the incandescence signal from the rBC (Moteki and Kondo, 2007). The bimodal distribution of lag-time could be reasonably fitted by combination of two Gaussian functions. The lag-time value of the uncoated fullerene soot particle employed in the calibration was 0.8 ± 0.5 μs, indicating that uncoated BC particles also should be within this range. Therefore, lag-time peaks for rBC with a diameter of 200 ± 10 nm in the range 0.6–1.0 μs and 2.3–2.6 μs in Figure 6b should be non/less-coated and thickly-coated, respectively. The fractions of thickly-coated rBC were 73%, 65%, 81%, and 88% for samples A, B, C, and D, respectively, while the peak lag-times of non/less-coated rBC and thickly-coated rBC were similar for all samples. The greater count fraction of thickly-coated BC for samples C and D compared to those for samples A and B was consistent with the expectation based on the trajectories of the air masses: samples C and D were considered to be influenced mainly by continental outflow and samples A and B were likely influenced by emissions from the main island of Japan.

3.3.2 Morphological types and mixing states

Figure 7 shows examples of electron microphotographs, at the same magnification, before and after EDS analysis of samples A and D. Most of the particles in all samples had a rounded

shape or were clustered into boll shapes. The round particles and spherical portions of clustered particles in sample A were smaller than those of sample D. Comparing particles before and after EDS, a large particle mass was evaporated or sublimated due to beam damage by the high density electron beam, while some chain-shaped residues (shown by black triangles in Figures 7a' and 7b'), which could be characterized as soot, were often found in the particles after EDS. In sample A, non-soot residues were also found in most particles after EDS. This non-soot residue mostly showed a weak contrast against the background collodion film, such as the materials shown by white triangles in Figure 7a'. A fraction of soot-like particles coexisted with the weakly contrasting residues. Particles of samples B and C resembled those of sample A and D, respectively.

According to the methods used by Ueda et al., (2011), the particles were classified into seven types based on their morphological features, as presented in Figure 8. The pie chart for each type (Figure 8) indicates the number fraction of particles for each compositional type based on EDS analysis. The number below the pie graph is the number of particles in each type. Detailed information on the classification and features of each morphological type and estimation of volume-equivalent diameter is described in the Supplemental Material (S2).

For type 2, 3, 4, and 5 particles, EDS analysis indicates that most were composed mainly of sulfate. However, some of them also contained carbon and sulfur, and the mixed ratio of carbon in the particle differed between particle types. The averaged peak intensity C to S ratio for sulfate-rich particles was 0.45, 0.13, 0.88, and 0.33 for types 2, 3, 4 and 5, respectively. This result suggests that coccoid sulfate (type 3) was less mixed with organic matter, while dome-like sulfate (type 4) was mixed with a larger amount of carbon.

The mixing states of particles were classified by comparing particle shape and morphology before and after irradiation by the high, densely-intense electron beam of the EDS analysis. Some materials, such as ammonium sulfate and sulfuric acid, evaporate or sublimate due to irradiation by the intense electron beam, whereas non-volatile materials, including soot, sea salt, and crustal particles, remain on the film after irradiation (e.g., Li et al., 2003, 2010; Pósfai et al., 2003; Adachi et al., 2014). The types of mixing states are shown in Figure 9. Detailed information on the classification of mixing states is described in the Supplemental Material (S3). Based on the EDS analysis, type *a* particles are composed mainly of carbon and silicate. Type *b* particles were mostly classified as sulfate-rich, sea salt-rich, or aged sea salt-rich. For the sulfate-rich type *b* particles, the C to S ratios in the peak intensities were

relatively high (0.99 on average), suggesting that they also contained a large amount of carbonaceous material. The majority of the type *c*, *d*, *e*, and *f* particles were classified as sulfate-rich particles. The averaged C to S ratios in the peak intensities for sulfate-rich particles were 0.40, 0.45, 0.71, and 0.10 for types *c*, *d*, *e*, and *f*, respectively; type *e* particles contained relatively large amounts of carbon, whereas type *f* particles were composed mostly of sulfate. Similar particles to those of type *e* were also found, and regarded as organics, during observation of the Chinese continental outflow (Li et al., 2013).

Figures 10a and b show size-segregated number proportions of the mixing states and morphological types of the particles in samples A–D on the basis of the classification in Figs. 9 and 8, respectively. The mixing states had two patterns: (1) a combination of type *c* (mixed particles of soot and volatile) and type *e* (semi-volatile) particles, as found in samples A and B; and (2) a combination of type *c* and type *f* (volatile) particles, as found in samples C and D. Comparing with the chemical compositions measured by ACSM, the proportion of type *e* particles to type *f* particles was higher in samples collected when the mass ratio of organics was relatively high. This corresponded with the ratio of C to S by EDS analysis for type *e* and *f* particles. The number proportion of soot-containing particles (types *a* and *c*) was about 10%–50% at each size range. Most soot was found as mixed particles with volatile materials. Morphological types of particles in all the samples (Figure 10b) were mainly of type 2 (spherical) in the smaller size range and type 5 (clustered) in the larger size range. Compared to samples A and B, the fraction of type 2 particles tended to be higher for samples C and D (0.3–0.6 μm).

Relatively large spherical and clustered sulfate-rich particles were found in aged air masses (samples C and D), as discussed in section 3.3.1. Similar spherical and clustered sulfate-rich particles were simultaneously observed in the Asian outflow at Cape Hedo (Ueda et al., 2011). Using a simple numerical model and meteorological conditions along the backward trajectories, Ueda et al. (2011) demonstrated that the presence of clustered particles under dry conditions was explained by coagulation processes over several days in polluted conditions. In the present study, spherical particles were simultaneously observed with clustered particles. In addition, the relative humidity along the backward air mass trajectories, which were computed using the HYSPLIT model, was lower than the deliquescence humidity of ammonium sulfate (80%) for about 1 day for sample A and about 2 days for samples B, C, and D before arrival at the site. Therefore, clustered particles would have been formed by

coagulation of spherical particles under dry conditions. The differences of spherical particle (and spherical parts of clustered particle) sizes among samples A–D might be attributed to the different sources and/or aging processes through the condensation of gaseous molecules.

Figure 10c shows size-segregated number proportions of the morphological types of soot-containing particles (i.e., types *a* and *c*) before EDS analysis. Number proportions for soot-containing particles show a similar tendency to those for all particles in Figure 10b. This indicates that the morphology of a large portion of soot-containing particles reflected the shape of the coating materials, while a portion of the soot-containing particles has a soot-aggregated shape (type 1) in samples A and B. The presence of the non/less-coated soot particles in samples A and B is consistent with the results obtained by the SP2 (Figure 6).

3.3.3 Internal mixing states and shape factors for soot-containing particles

The controlling factors of the lensing effect of a soot-containing particle include coating thickness, morphology and position of the soot, and composition of the coating materials. In this study, the shape factors for soot-containing particles (i.e., types *a* and *c*) were estimated by electron micrograph before and after irradiation with a high, densely-intense electron beam.

Table 3 lists average and 25th and 75th percentile values of parameters of the soot-containing particles (number, particle and soot diameter (d_p, d_s), volume fraction and relative position of soot (VF_s, RP), circularity factor (CF) and aspect ratio (AR)) for each sample. Details of image analysis and estimation of these parameters were described in the Supplemental Material (S4). The soot diameters d_s were 0.2–0.3 and 0.2–0.4 μm for particles with d_p of ≤ 0.6 and > 0.6 μm, respectively. The d_s values are roughly consistent with the diameter of rBC determined using SP2 (Figure 6a). The VF_s were 21%–50% and ~10% for particles with d_p of < 0.6 and > 0.6 μm, respectively. The VF_s values indicate that a large portion of the soot-containing particles were mixed with other materials. Although no significant differences in VF_s values among the samples were observed for particles with d_p of > 0.6 μm, the VF_s values for samples A and B were higher than those for samples C and D for particles with d_p of < 0.6 μm, likely due to the presence of the non/less-coated soot particles in samples A and B (as discussed in section 3.3.2). Low values of VF_s were also reported by observational studies at background and remote sites: for example, the average values (8%–28%) of the soot volume fraction for 0.15–0.8 μm particles at an urban background site in Mainz, Germany (Vester et

al., 2007) and median value (15%) of the soot volume fraction for 0.05–0.3 μm particles in Mexico City (Adachi and Buseck, 2008) and median values (< 20% for 0.2–0.4 μm and < 10% for 0.4–0.7 μm) of the insoluble soot volume fraction in Cape Hedo (Ueda et al., 2011).

The *CF* and *AR* represent shape factors. The averaged *CF* and *AR* values of samples C and D were near 1 (*CF* > 0.80 and *AR* < 1.3) for all size ranges, suggesting that a large fraction of the particles were near-spherical. Small *CF* values (< 0.4) were observed for particles with d_p of > 0.6 μm in samples A and B, likely due to the clustered morphology of the larger soot-containing particles (type 5, in Figure 10c).

The *RP* is an indicator of soot position in the particle. The averaged *RP* values were 0.4–0.6 and 0.6–0.9 for < 0.6 and > 0.6 μm particles, respectively. These values indicate that most of the soot was inside the sphere-equivalent diameter but not at the center of the particle. Our averaged *RP* values were almost equal to the average values (0.54) of soot particle position for 0.05–0.3 μm particles in Mexico City (Adachi et al., 2010). It should be noted that the *RP* value was estimated with reference to the sphere-equivalent diameter in our method. Therefore, the *RP* values for particles with an irregular shape can be less than 1 even if soot is attached/partly-embedded on/in other materials.

Internal mixing states of the soot-containing particles were also classified, directly from the microphotograph, into three types: type *a* (non/less coated soot), an attached/partly-embedded type, and a coated type (Table 4). Particles were classified to the attached/partly-embedded type if at least part of the soot in a type *c* particle was apparent in the microphotograph before EDS analysis; otherwise, the particle was classified as the coated type. For samples A and B, the number fraction of attached/partly-embedded soot was about 30% for < 0.6 μm particles and 60%–70% for > 0.6 μm particles. For samples C and D, most of the soot (> 83%) was classified as the coated type. Soot-containing particles in samples A and B had more irregular shapes than those in samples C and D, although no clear difference in averaged *RP* values among the samples was found. These results suggested that the soot in samples A and B would not be thickly coated compared to that in samples C and D. Several observational studies of soot-containing particles using microscopy also found some attached/partly-embedded soot on/in sulfate-rich particles (Jonson et al., 2005; Shi et al., 2008; Adachi and Buseck, 2013).

3.4 Comparison of optical properties with mixing states and morphological features

As mentioned in Section 3.1, the E_{abs} values tended to be smaller at shorter wavelengths, possibly due to the formation of brownish materials in the TDs maintained at 300 °C or 400 °C. In this study, several samples for morphological analysis were collected after passing the particles through the TD maintained at 400 °C. Figure 12 shows an example electron micrograph of such particles. These were sampled just after the collection of sample A on May 6 when a small E_{abs}(405 nm) value (0.88) was observed (Table 2). Based on EDS analysis, some carbon-rich particles were found. The morphologies of the carbon-rich particles not only had a chain-like shape but were also spherical. These particles were not evaporated during irradiation by the high density electron beam of the EDS analysis. The spherical particle features (*i.e.*, non-volatile, spherical, and carbon-rich) were similar to tar ball, which is originated in biomass burning (Pósfai et al., 2003, 2004; Alexander et al., 2008; Adachi and Buseck, 2011). Alexander et al. (2008) quantified the optical properties of similar amorphous carbon sphere particles in the East Asian-Pacific outflow using the electron energy-loss spectrum in TEM, and indicated that these particles have strong light absorption, with mean refractive indices of 1.67–0.27*i* at 550 nm. Although these carbon-rich, spherical, non-volatile particles were rare in our samples collected without passing the particles through the TD, a large number of particles in samples A and B had non-volatile residues after EDS analysis (type *e*, in Figure 10a). Therefore, the spherical, carbon-rich particles might be formed by heating, probably due to the incomplete charring of organic compounds, and could be brown in colour.

In contrast, the formation of brownish materials was not observed in our previous study at an urban area in Nagoya, although the same procedure was used to determine the wavelength dependent E_{abs} values (Nakayama et al., 2014). During the observations at Nagoya in August, most of the heated particles were found to be non-spherical (based on the effective density distribution measurements (Nakayama et al., 2014)). Differences in the source and degree of aging of carbonaceous particles may contribute to the observed difference in the wavelength dependence of E_{abs}. Our results suggest that attention needs to be paid when a TD is used to estimate the contributions of the lensing effect and brown carbon, especially for particles in aged air masses.

In this study, to avoid the possible contributions of the formation of brownish particles in the TD, E_{abs}(781 nm) is used for discussion of the lensing effect. The average E_{abs}(781 nm) values observed in this study (1.22 and 1.23 at 300 and 400 °C, respectively, Table 1) was larger than the values reported by Cappa et al. (2012) around large cities in California during early summer (on average 1.06 at 532 nm) and by Nakayama et al. (2014) in an urban area at Nagoya, Japan during August (on average 1.10 at 781 nm), likely because relatively aged particles were observed in this study. Very recently, Liu et al. (2015) reported the average E_{abs}(781 nm) of 1.4 for BC particles emitted from fossil fuel and residential burning sources in winter at a rural site, Detling (45 km away from London) in UK. The average E_{abs}(781 nm) value obtained in the present study is slightly lower than the value reported by Liu et al. (2015).

Most of the soot-containing particles in all the samples under high absorption coefficient conditions were internally-mixed with a large amount (> 50% of particle volume) of other materials (Table 3). Previous models based on Mie theory and assuming a core-shell (the BC core and coating materials) shape suggested E_{abs} values larger than 1.5 when particles had a heavy coating (Bond et al., 2006). The average E_{abs} value observed in this study was still smaller than the estimation assuming core-shell morphology. Adachi et al. (2010) estimated the lensing effect of irregularly shaped particles and those with an assumed core-shell shape, and reported that the difference in the calculated absorption was related to the position of soot in the particle and the fractal dimension. Based on their results, absorption of soot-containing particles with our averaged *RP* values (0.4–0.9) could be about 10%–25% smaller than the value estimated assuming core-shell morphology. The position of soot in the particle may contribute to the difference between observation and estimation, as previously suggested by Cappa et al. (2012).

Comparing among pollution events in this study, the E_{abs}(781 nm) values for the long range transported continental outflow (May 13 and 14) were larger (> 1.3) than those for the air masses likely affected by emissions from the main island of Japan (May 6 and 10), as listed in Table 2. These results are consistent with the results of the SP2 and TEM analyses. Greater count fractions of thickly-coated BC were observed in the SP2 measurements (Figure 6), and a greater number fraction of coated soot particles (Table 3) and lower volume fraction of soot in smaller particles (< 0.6 μm) (Table 4) were observed in samples C and D compared to samples A and B. In addition, number fractions of coated soot particles were greater during

the high E_{abs} events (samples C and D) compared to samples A and B (Table 5). The greater circularity of the soot-containing particles in samples C and D (Table 4, Figure 10c) may also contribute to the greater E_{abs} values, as discussed by Adachi et al. (2010). Although most soot-containing particles in all samples in this study were internally mixed with sulfate and organics, the number fraction of thickly-coated soot was higher in more aged air masses from China. Our results indicate that, according to the transport pathway and aging levels of the air mass, the magnitude of the lensing effect could change with changes in the mixing states and morphology of soot-containing particles.

4 Summary and Conclusions

To elucidate the lensing effect of aged BC particles and their relation with the mixing state and morphology of individual particles, *in situ* measurements of the optical and chemical properties and size distributions of aerosols and the mixing state of rBC, as well as sampling for TEM analysis, were conducted at an Asian outflow site in Noto Peninsula, Japan, in spring 2013.

The enhancement factor, $E_{abs}(\lambda)$, at 405, 532, and 781 nm was determined by comparing the light absorption of aerosol particles with and without passing through a TD maintained at 300 °C or 400 °C. The E_{abs} values tended to be lower at shorter wavelengths. In samples exhibiting a relatively small enhancement of light absorption at 405 nm after passage of the particles through the TD (samples A and B), spherical, carbon-rich particles were found, implying that the brownish materials may be formed during the heating processes.

The E_{abs}(781 nm) values estimated using the data at the TD temperature of 300 °C, which was assumed to represent the magnitude of the lensing effect, was 1.22 on average. Large E_{abs}(781 nm) values (> 1.3) were observed on May 13–14 when the air mass was transported over 2–3 days from urban areas in China. In the samples collected on May 13–14 (samples C and D), most soot-containing particles were internally mixed with a large amount of coating materials involving sulfate. Results of SP2 measurement and TEM analyses indicated that the number proportion of thickly-coated soot particles tended to be grater in these air masses. In addition, most soot-containing particles in samples C and D were close to a spherical shape, whereas larger number fractions of soot-containing particles were mixed with cluster of sulfate containing spherules in samples A and B. These results suggest that the mixing state and

morphological features of soot-containing particles would be factors controlling the lensing effect of BC in this study. The relation between the magnitude of the lensing effect and the mixing state and morphology of individual soot-containing particles for well-aged air masses will be useful to evaluate the direct radiative forcing of aerosols, particularly in leeward areas of large emission sources of BC.

Acknowledgements

We express our gratitude to Ms. M. Sawano, Ms. S. Kagami (Kanazawa Univ.), and Mr. T. Yamasaki (Nagoya Univ.) for assisting our research. We gratefully acknowledge the NOAA Air Resources Laboratory (ARL) for providing the HYSPLIT transport model (http://www.arl.noaa.gov/ready.html). This work was performed with the support of the Grant-in-Aid for Scientific Research (KAKENHI 25701001 and 25740013) and Green Netwaork of Excellence, Environmental Information (GRENE-ei) program from the Ministry of Education, Culture, Sports, Science and Technology (MEXT), the Global Environment Research Fund (2-1403) of the Ministry of the Environment, Japan, Toyoaki Scholarship Foundation, and the joint research program of the Solar-Terrestrial Environment Laboratory, Nagoya University.

References

Adachi, K. and Buseck, P. R.: Internally mixed soot, sulfates, and organic matter in aerosol particles from Mexico City, Atmos. Chem. Phys., 8, 6469–6481, doi:10.5194/acp-8-6469-2008, 2008.

Adachi, K. and Buseck, P. R.: Atmospheric tar balls from biomass burning in Mexico, J. Geophys. Res. Atmos., 116, D5, doi: 10.1029/2010JD015102 , 2011.

Adachi, K. and Buseck, P. R.: Changes of ns-soot mixing states and shapes in an urban area during CalNex, J. Geophys. Res. Atmos., 118, 3723–3730, doi: 10.1002/jgrd.50321, 2013.

Adachi, K., Chung, S. H., and Buseck, P. R.: Shapes of soot aerosol particles and implications for their effects on climate, J. Geophys. Res., 115, D15206, doi:10.1029/2009JD012868, 2010.

Adachi, K., Zaizen, Y., Kajino, M., and Igarashi, Y.: Mixing state of regionally transported soot particles and the coating effect on their size and shape at a mountain site in Japan, J. Geophys. Res. Atmos., 119, 5386–5396, doi: 10.1002/2013JD020880, 2014.

Alexander, D. T. L., Crozier, P. A., and Anderson, J. R.: Brown carbon spheres in East Asian outflow and their optical properties, Science, 321, 833–836, doi: 10.1126/science.1155296, 2008.

Andreae, M. O. and Gelencsé, A.:, Black carbon or brown carbon? The nature of light-absorbing carbonaceous aerosols, Atmos. Chem. Phys., 6, 3131–3148, 2006.

Bond, T. C., and Bergstrom, R. W.: Light absorption by carbonaceous particles: An investigative review, Aerosol Sci. Tech., 40, 27–67, doi: 10.1080/02786820500421521, 2006.

Bond, T. C., Streets, D. G., Yarber, K. F., Nelson, S. M., Woo, J.-H., and Klimont, Z.: A technology-based global inventory of black and organic carbon emissions from combustion, J. Geophys. Res., 109, D14203, doi: 10.1029/2003JD003697, 2004.

Bond, T. C., Habib, G., and Bergstrom, R. W.: Limitations in the enhancement of visible light absorption due to mixing state, J. Geophys. Res., 111, D20211, doi:10.1029/2006JD007315, 2006.

Bond, T. C., Doherty, S. J., Fahey, D. W., Forster, P. M., Berntsen, T., DeAngelo, B. J., Flanner, M. G., Ghan, S., Kärcher, B., Koch, D. Kinne, S., Kondo, Y., Quinn, P. K., Sarofim, M. C., Schultz, M. G., Schulz, M., Venkataraman, C., Zhang, H., Zhang, S., Bellouin, N.,

Guttikunda, S. K., Hopke, P. K., Jacobson, M. Z., Kaiser, J. W., Klimont, Z., Lohmann, U., Schwarz, J. P., Shindell, D., Storelvmo, T., Warren, S. G., and Zender, C. S.:, Bounding the role of black carbon in the climate system: A scientific assessment, J. Geophys. Res. Atmos., 118, 5380–5552, doi: 10.1002/jgrd.50171, 2013.

Cappa, C. D., Onasch, T. B., Massoli, P., Worsnop, D. R., Bates, T. S., Cross, E. S., Davidovits, P., Hakala, J., Hayden, K. L., Jobson, B. T., Kolesar, K. R., Lack, D. A., Lerner, B. M., Li, S. M., Mellon, D., Nuaaman, I., Olfert, J. S., Petaja, T., Quinn, P. K., Song, C., Subramanian, R., Williams, E. J., and Zaveri, R. A.: Radiative absorption enhancements due to the mixing state of atmospheric black carbon, Science, 337, 1078–1081, doi:10.1126/science.1223447, 2012.

Chan, T. W., Brook, J. R., Smallwood, G. J., and Lu, G.: Time-resolved measurements of black carbon light absorption enhancement in urban and near-urban locations of southern Ontario, Canada, Atmos. Chem. Phys., 11, 10407-10432, doi:10.5194/acp-11-10407-2011, 2011.

Draxler, R. R. and Rolph, G. D., 2003. HYSPLIT (HYbrid Single-Particle Lagrangian Integrated Trajectory) Model access via NOAA ARL READY Website, available at: http://www.arl.noaa.gov/ready/hysplit4.htm (last access: October 3, 2013), NOAA Air Resources Laboratory, Silver Spring, MD.

Fuchs, N.A.: The coagulation of aerosols, in The mechanics of aerosols, pp. 288–322, Dover Publications, Inc., New York, 1964.

Gao, R. S., Schwarz, J. P., Kelly, K. K., Fahey, D. W., Watts, L. A., Thompson, T. L., Spackman, J. R., Slowik, J. G., Cross, E. S., Han, J. H., Davidovits, P., Onasch, T. B., and Worsnop, D. R.: A novel method for estimating light-scattering properties of soot aerosols using a modified single-particle soot photometer, Aerosol Sci. Tech., 41, 125–135, doi:10.1080/02786820601118398, 2007.

Guo, X., Nakayama a, T., Yamada, H., Inomata, S., Tonokura, K., and Matsumi, Y.: Measurement of the light absorbing properties of diesel exhaust particles using a three-wavelength photoacoustic spectrometer, Atmos. Environ., 94, 428–437, doi:10.1016/j.atmosenv.2014.05.042, 2014.

Hasegawa. S. and Ohta, S.: Some measurements of the mixing state of soot-containing particle at urban and non-urban sites, Atmos. Environ., 36, 3899–3908, doi:10.1016/S1352-2310(02)00343-6, 2002.

Healy, R. M., Wang, J. M., Jeong, C.-H., Lee, A. K. Y., Willis, M. D., Jaroudi, E., Zimmerman, N., Hilker, N., Murphy, M., Eckhardt, S., Stohl, A., Abbatt, J. P. D., Wenger, J. C., and Evans, G. J., Light-absorbing properties of ambient black carbon and brown carbon from fossil fuel and biomass burning sources, J. Geophys. Res. Atmos., 120, 6619-6633, doi:10.1002/2015JD023382, 2015.

Husar, R.B. and Whitby, K.T.: Growth Mechanisms and size spectra of photochemical aerosols. Environ. Sci. Tech. 7, 241–247, doi: 10.1021/es60075a003, 1973.

Intergovernmental Panel on Climate Change (IPCC), Climate Change 2013: The Physical Science Basis, Cambridge Univ. Press, Cambridge, UK., 2013.

Iseki, S., Sadanaga, Y., Matsuki, A., Iwasaka, Y., Sato, K., Takenaka, N., and Bandow H.: Analyses of the concentration variations of ozone and carbon monoxide at Suzu, the Noto Peninsula, J. Jpn. Soc. Atmos. Environ., 45, 256–263, doi: 10.11298/taiki.45.256, 2010. (in Japanese)

Ishiyama, A., Takaji, R., Sadanaga, Y., Matsuki, A., Sato, K., Osada, K., and Bandow, H.: Seasonal variations of peroxyacyl nitrates and alkyl nitrates concentrations at Suzu, the Noto Peninsula, J. Jpn. Soc. Atmos. Environ., 50, 16-26, 2015. (in Japanese)

Johnson, K. S., Zuberi, B, Molina, L. T., Molina, M. J., Iedema, M. J., Cowin, J. P., Gaspar, D. J., Wang, C., and Laskin, A.: Processing of soot in an urban environment: case study from the Mexico City Metropolitan Area, Atmos. Chem. Phys., 5, 3033–3043, doi:10.5194/acp-5-3033-2005, 2005.

Knox, A., Evans, G. J., Brook, J. R., Yao, X., Jeong, C.-H., Godri, K. J., Sabaliauskas, K., and Slowik, J. G.: Mass absorption cross-section of ambient black carbon aerosol in relation to chemical age, Aerosol Sci. Technol., 43, 522–532, doi:10.1080/02786820902777207., 2009.

Kurokawa, J., Ohara, T., Morikawa, T., Hanayama, S., Greet, J.-M., Fukui, T., Kawashima, K., and Akimoto, H.: Emissions of air pollutants and greenhouse gases over Asian regions during 2000–2008: Regional Emission inventory in ASia (REAS) version 2, Atmos. Chem. Phys., 13, 11019–11058, doi:10.5194/acp-13-11019-2013, 2013.

Ma, X., Yu, F., and Luo, G.: Aerosol direct radiative forcing based on GEOS-Chem-APM and uncertainties, Atmos. Chem. Phys., 12, 5563–5581, doi:10.5194/acp-12-5563-2012, 2012.

Lack, D. A. and Cappa, C. D.: Impact of brown and clear carbon on light absorption enhancement, single scatter albedo and absorption wavelength dependence of black carbon, Atmos. Chem. Phys., 10, 4207–4220, doi:10.5194/acp-10-4207-2010, 2010.

Lack, D. A., Langridge, J. M., Bahreini, R., Cappa, C. D., Middlebrook, A. M., and Schwarz, J. P.: Brown carbon and internal mixing in biomass burning particles, Proc. Natl. Acad. Sci. USA, 109, 14802–14807, doi: 10.1073/pnas.1206575109, 2012.

Li, J., Pósfai, M., Hobbs, P. V., and Buseck, P. R.: Individual aerosol particles from biomass burning in southern Africa: 2, Compositions and aging of inorganic particles, J. Geophys. Res., 108, D13, 8484, doi:10.1029/2002JD002310, 2003.

Li, W. J., Shao, L. Y., and Buseck, P. R.: Haze types in Beijing and the influence of agricultural biomass burning, Atmos. Chem. Phys., 10, 8119–8130, doi:10.5194/acp-10-8119-2010, 2010.

Li, W., Wand, T., Zhou, S., Lee, S. C., Huang, Y., Gao, Y., and Wang, W.: Microscopic observation of metal-containing particles from Chinese continental outflow observed from a Non-Industrial Site, Environ. Sci. Tech., 4, 9124–9131, doi: 10.1021/es400109q, 2013.

Liu, S. Aiken, A. C., Gorkowski, K., Dubey, M. K., Cappa, C. D., Williams, L. R., Herndon, S. C., Massoli, P., Fortner, E. C., Chhabra, P. S., Brooks, W. A., Onasch, T. B., Jayne, J. T., Worsnop, D. R., China, S., Sharma, N., Mazzoleni, C., Xu, L., Ng, N. L., Liu, D., Allan, J. D., Lee, J. D., Fleming, Z. L., Mohr, C., Zotter, P., Szidat, S., and Prévôt, A. S. H., Enhanced light absorption by mixed source black and brown carbon particles in UK winter, Nature Comm., 6, 8435, doi:10.1038/ncomms9435, 2015.

Ma, X., Yu, F., and Luo, G.: Aerosol direct radiative forcing based on GEOS-Chem-APM and uncertainties, Atmos. Chem. Phys., 12, 5563–5581, doi:10.5194/acp-12-5563-2012, 2012.

Maki, T., Susuki, S., Kobayashi, F., Kakikawa, M., Tobo, Y., Yamada, M., Higashi, T., Matsuki, A., Hong, C., Hasegawa, H., and Iwasaka, Y.: Phylogenetic analysis of atmospheric halotolerant bacterial communities at high altitude in an Asian dust (KOSA) arrival region, Suzu City, Sci. Total Environ., 408, 4556–4562, doi:10.1016/j.scitotenv.2010.04.002, 2010.

Mamane, Y. and Gottlieb, J.: The study of heterogeneous reactions of carbonaceous particles with sulfur and nitrogen oxides using single particles. J. Aerosol. Sci. 20, 575–584, doi:10.1016/0021-8502(89)90104-3, 1989.

Meng, Z. and Seinfeld, J.H.: On the source of submicrometer droplet mode of urban and regional aerosols. Aerosol Sci. Tech., 20, 253–265.1994.

Moosmüller, H., Chakrabarty, R. K., and Arnott, W. P.: Aerosol light absorption and itsmeasurement: A review, J. Quant. Spectrosc. Radiat. Transfer, 110, 844–878, doi:10.1016/j.jqsrt.2009.02.035, 2009.

Moteki, N. and Kondo, Y.: Effects of Mixing State on Black Carbon Measurements by Laser-Induced Incandescence, Aerosol Sci. Tech., 41, 398–417, doi: 10.1080/02786820701199728, 2007.

Murr, L. E. and Soto, K. F.: A TEM study of soot, carbon nanotubes, and related fullerene nanopholyhedra in common fuel-gas combustion sources, Mater. Charact., 55, 50–65. 2005.

Nakayama, T., Sato, K., Matsumi, Y., Imamura, T., Yamazaki, A., and Uchiyama, A.: Wavelength and NO_x dependent complex refractive index of SOAs generated from the photooxidation of toluene, Atmos. Chem. Phys., 13, 531–545, doi:10.5194/acp-13-531-2013, 2013.

Nakayama, T., Ikeda, Y., Sawada, Y., Setoguchi, Y., Ogawa, S., Kawana, K., Mochida, M., Ikemori, F., Matsumoto, K., and Matsumi, Y.: Properties of light-absorbing aerosols in the Nagoya urban area, Japan, in August 2011 and January 2012: Contributions of brown carbon and lensing effect, J. Geophys. Res. Atmos., 119, 12721–12739, doi:10.1002/2014JD021744, 2014.

Nakayama, T., Suzuki, H., Kagaminani, S., Ikeda, Y., Uchiyama, A., and Matsumi, Y.: Characterization of a three wavelength photoacoustic soot spectrometer (PASS-3) and a photoacoustic extinctiometer (PAX), J. Metorol. Soc. Jpn., 93, 285-308, doi:10.2151/jmsj.2015-016, 2015.

Ng , N. L., Herndon, S. C., Trimborn, A., Canagaratna, M. R., Croteau, P. L., Onasch, T. B., Sueper, D., Worsnop, D. R., Zhang, Q., Sun, Y. L., and Jayne, J. T.: An Aerosol Chemical Speciation Monitor (ACSM) for Routine Monitoring of the Composition and Mass Concentrations of Ambient Aerosol, Aerosol Sci. Tech., 45, 780–794, doi: 10.1080/02786826.2011.560211, 2011

Okada, K.: Nature of individual hygroscopic particles in the urban atmosphere. J. Meteor. Soc. Japan, 61, 727–735, 1983.

Ohara, T., Akimoto, H., Kurokawa, J., Horii, N., Yamaji, K., Yan, X., and Hayasaka, T.: An Asian emission inventory of anthropogenic emission sources for the period 1980–2020, Atmos. Chem. Phys., 7, 4419–4444, doi:10.5194/acp-7-4419-2007, 2007.

Pósfai, M., Anderson, J. R., and Buseck, P. R.: Soot and sulfate aerosol particles in the remote marine troposphere, J. Geophys. Res., 104, D17, 685–693, doi: 10.1029/1999JD900208, 1999.

Pósfai, M., R. Simonics, Li, J., Hobbs, P. V., and Buseck, P. R..: Individual aerosol particles from biomass burning in southern Africa: 1. Compositions and size distributions of carbonaceous particles, J. Geophys. Res., 108, D13, doi:10.1029/2002JD002291, 2003.

Pósfai, M., Gelencser, A., Simonics, R., Arato, K., Li, J., Hobbs, P. V., and Buseck, P. R.: Atmospheric tar balls: Particles from biomass and biofuel burning, J. Geophys. Res., 109, D06213, doi: 10.1029/2003JD004169, 2004.

Ramanathan, V. and Carmichael, G.: Global and regional climate changes due to black carbon, Nature Geoscience, 1, 221–227, doi:10.1038/ngeo156, 2008.

Rolph, G. D., 2003. Real-time environment applications and display system (READY), NOAA Air Resour. Lab., Silver Spring, Md., Available at: http://www.arl.noaa.gov/ready/hysplit4.html (last access: October 3, 2013)

Sadanaga, Y., Yuba, A., Kawakami, J., Takenaka, N., Yamamoto, M., and Bandow, H.: A gaseous nitric acid analyzer for the remote atmosphere based on the scrubber difference/NO-ozone chemiluminescence method, Anal. Sci., 24, 967–971, doi: 10.2116/analsci.24.967, 2008.

Sadanaga, Y., Fukumori, Y., Kobashi, T., Nagata, M., Takenaka, N., and Bandow, H.: Development of a selective light-emitting diode photolytic NO_2 converter for continuously measuring NO_2 in the atmosphere, Anal. Chem., 82, 9234-9239, doi:10.1021/ac101703z, 2010.

Shi, Z., Zhang, D., Ji, H., Hasegawa, S., and Hayashi, M.: Modification of soot by volatile species in an urban atmosphere, Sci. Total, Environ., 389, 195 –201, doi:10.1016/j.scitotenv.2007.08.016, 2008.

Streets, D.G., Bond, T. C., Carmichael, G. R., Fernandes, S. D., Fu, Q., He, D., Klimont, Z., Nelson, S. M., Tsai, N. Y., Wang, M. Q., Woo, J.-H., and Yarber, K. F.: An inventory of gaseous and primary aerosol emissions in Asia in 2000, J. Geophys. Res., 108, D21, doi:10.1029/2002JD003093, 2003.

Takami, A., Miyoshi, T., Shimono, A., and Hatakeyama, S. : Chemical composition of fine aerosol measured by AMS at Fukue Island, Japan during APEX period, Atmos. Environ., 39, 4913–4924, doi:10.1016/j.atmosenv.2005.04.038, 2005.

Takami, A., Miyoshi, T., Shimono, A., Kaneyasu, N., Kato, S., Kajii, Y., and Hatakeyama, S. : Transport of anthropogenic aerosols from Asia and subsequent chemical transformation, J. Geophys. Res., 112, D22S31, dio:10.1029/2006JD008120, 2007.

Ueda, S., Osada, K., and Takami, A.: Morphological features of soot-containing particles internally mixed with water-soluble materials in continental outflow observed at Cape Hedo, Okinawa, Japan. J. Geophys. Res. 116, doi: 10.1029/2010JD015565, 2011.

Ueda, S., Hirose, Y., Miura, K., and Okochi, H.: Individual aerosol particles in and below clouds along a Mt. Fuji slope: Modification of sea-salt-containing particles by in-cloud processing, Atmos. Res., 137, 216–227, D17207, doi:10.1016/j.atmosres.2010.10.021, 2014.

Vester, B. P., Ebert, M., Barnert, E. B., Schneider, J., Kandler, K., Schütz, L., and Weinbruch, S.: Composition and mixing state of the urban background aerosol in the Rhein-Main area (Germany), Atmos. Environ., 41, 6102–6115, doi:10.1016/j.atmosenv.2007.04.021, 2007.

Weingartner. E., Burtscher, H., and Baltensperger, U.: Hygroscopic properties of carbon and diesel soot particles, Atmos. Environ., 31, 2311–2327, doi:10.1016/S1352-2310(97)00023-X, 1997.

Yang, H. and Yu, Z.: Uncertainties in charring correction in the analysis of elemental and organic carbon in atmospheric particles by thermal/optical methods, Environ. Sci. Tech., 36, 5199–5204, doi: 10.1021/es025672z, 2002.

Yu, J. Z., Xu, J., and Yang, H.: Charring characteristics of atmospheric organic particulate matter in Thermal Analysis, Environ. Sci. Tech., 36, 754–761, doi:10.1021/es015540q, 2002.

Yuba, A., Sadanaga, Y., Takami, A., Hatakeyama, S., Takenaka, N., and Bandow, H.: Measurement system for particulate nitrate based on the scrubber difference NO-O_3

chemiluminescence method in remote areas, Anal. Chem., 82, 8916–8921, doi: 10.1021/ac101704w, 2010.

Yuba, A., Sadanaga, Y., Takami, A., Hatakeyama, S., Takenaka, N., Yoshihiko, M., Ohara, T., Yonemura, S., Kato, S., Kajii, Y., and Bandow, H.: Concentration variations of total reactive nitrogen and total nitrate during transport to Fukue Island and to Cape Hedo, Japan in the marine boundary layer, Atmos. Environ., 97, 471–478, doi:10.1016/j.atmosenv.2014.04.010, 2014.

Zuberi, B., Johnson, K. S., Aleks, G. K., Molina, L. T., and Molina, M. J.: Hydrophilic properties of aged soot, Geophys. Res. Lett., 32, L01807, doi:10.1029/2004GL021496, 2005.

Table 1. Average values of absorption and scattering coefficients and enhancement of absorption during the observation period [a]

λ	$b_{abs}(\lambda)$	$b_{sca}(\lambda)$	$E_{abs}(\lambda, 300°C)$ [b]	$E_{abs}(\lambda, 400°C)$ [b]
405 nm	3.1 [1.3–4.6]	51.9 [23.5–70.1]	0.98 [0.85–1.09]	0.99 [0.87–1.06]
532 nm	2.7 [1.2–3.8]	---	1.06 [0.90–1.20]	1.06 [0.93–1.20]
781 nm	1.7 [0.8–2.4]	16.1 [7.3–17.4]	1.22 [1.07–1.38]	1.23 [1.10–1.35]

[a] Values in square brackets show the 25^{th} –75^{th} percentile range.

[b] Only the data above the detection limit were used in the calculation.

Table 2. TEM samples used in this study, and rBC, NO_x, and NO_y concentrations and optical parameters (average values ± standard deviation) during the sampling periods

TEM sample						
	ID		A	B	C	D
	Date		6-May	10-May	13-May	14-May
	Starting local time		9:10	10:09	16:00	8:29
	Collection time		7 min	7 min	10 min	6 min
	Analyzed particle number		586	296	226	412
SP2						
	rBC mass	[ngm^{-3}]	424 ± 11	403 ± 30	520 ± 28	597 ± 21
ACSM						
	Org	[μgm^{-3}]	6.20	8.81	-	7.64
	NH_4^+	[μgm^{-3}]	1.45	1.52	-	5.87
	SO_4^{2-}	[μgm^{-3}]	2.02	2.10	-	17.46
	NO_3^-	[μgm^{-3}]	0.34	1.72	-	1.05
	Cl^-	[μgm^{-3}]	0.03	nd	-	nd
	Total mass	[μgm^{-3}]	10.05	14.15	-	32.01
NO_x, NO_y						
	NO_x	[ppbv]	1.6 ± 0.9	3.7 ± 1.7	1.3 ± 0.1	1.0 ± 0.1
	NO_y	[ppbv]	3.4 ± 0.9	5.3 ± 1.5	3.5 ± 0.2	4.0 ± 0.2
	$[NO_x]/[NO_y]$		0.43 ± 0.12	0.67 ± 0.11	0.38 ± 0.03	0.24 ± 0.03
PASS-3						
	b_{abs}	[Mm^{-1}] 405 nm	6.3 ± 0.6	5.6 ± 1.2	7.9 ± 0.8	9.4 ± 0.2
		532 nm	4.6 ± 2.1	4.4 ± 0.6	6.0 ± 0.6	8.2 ± 0.4
		781 nm	2.8 ± 0.3	1.9 ± 0.6	3.5 ± 0.6	4.7 ± 0.2
	b_{sca}	[Mm^{-1}] 405 nm	99.8 ± 7.4	79.0 ± 4.1	155.8 ± 5.0	215.1 ± 1.9
		781 nm	27.3 ± 4.7	35.6 ± 17.3	69.2 ± 2.9	120.7 ± 2.5
	E_{abs}(300°C)	405 nm	0.88 ± 0.12	0.97 ± 0.26	1.33 ± 0.21	1.35 ± 0.06
		532 nm	1.31 ± 0.60	1.09 ± 0.40	1.42 ± 0.24	1.18 ± 0.20
		781 nm	1.25 ± 0.37	1.13 ± 0.49	1.44 ± 0.23	1.42 ± 0.18
	E_{abs}(400°C)	405 nm	0.88 ± 0.12	1.03 ± 0.25	1.22 ± 0.13	1.31 ± 0.06
		532 nm	1.05 ± 0.15	1.13 ± 0.36	1.10 ± 0.12	1.43 ± 0.38
		781 nm	1.26 ± 0.29	1.24 ± 0.60	1.58 ± 0.20	1.52 ± 0.19

Table 3. Parameters of the soot-containing particles of TEM samples [a]

ID		Number of soot particles	Particle diameter d_p [μm]	Soot diameter d_s [μm]	Volume fraction of soot VF_s [%]	Relative position of soot *RP*	Circularity factor *CF*	Aspect ratio *AR*
A	<0.6 μm	99	0.36 [0.26-0.45]	0.22 [0.16-0.25]	33 [10-50]	0.55 [0.30-0.74]	0.73 [0.59-0.93]	1.4 [1.1-1.6]
	>0.6 μm	10	0.83 [0.67-0.83]	0.36 [0.28-042]	11 [6-14]	0.89 [0.75-1.02]	0.34 [0.26-0.40]	2.1 [1.8-2.4]
B	<0.6 μm	33	0.36 [0.26-0.47]	0.20 [0.15-0.24]	50 [7-55]	0.48 [0.29-0.68]	0.60 [0.52-0.73]	1.4 [1.2-1.5]
	>0.6 μm	18	0.89 [0.73-1.07]	0.37 [0.21-0.55]	13 [2-16]	0.61 [0.42-0.79]	0.39 [0.21-0.56]	1.4 [1.2-1.5]
C	<0.6 μm	6	0.58 [0.57-0.59]	0.32 [0.22-0.40]	21 [5-31]	0.42 [0.28-0.58]	0.86 [0.84-0.88]	1.2 [1.1-1.2]
	>0.6 μm	75	0.92 [0.73-1.04]	0.33 [0.22-0.37]	9 [2-10]	0.44 [0.24-0.64]	0.81 [0.75-0.92]	1.2 [1.1-1.4]
D	<0.6 μm	86	0.47 [0.42-0.51]	0.23 [0.17-0.30]	22 [5-27]	0.55 [0.25-0.66]	0.89 [0.87-0.94]	1.1 [1.0-1.2]
	>0.6 μm	80	0.87 [0.71-1.02]	0.28 [0.14-0.35]	10 [1-12]	0.63 [0.38-0.87]	0.80 [0.70-0.92]	1.3 [1.1-1.5]

[a] Values in square brackets are show the 25^{th}–75^{th} percentile values

Table 4. Number fraction of mixing type of soot for soot-containing particles [%]

ID		Type a	Type c	
			Attached/partly-embedded	coated
A	<0.6μm	9	29	62
	>0.6μm	0	70	30
B	<0.6μm	12	33	55
	>0.6μm	0	61	39
C	<0.6μm	0	0	100
	>0.6μm	0	17	83
D	<0.6μm	0	5	95
	>0.6μm	0	10	90

Figure Captions

Figure 1. Flow diagram of a measurement system for dried particles that did and did not pass through the thermodenuders (TDs) maintained at 300 and 400 °C using the PASS-3, SMPS, and SP2. Black arrow lines indicate the flow lines of sample air.

Figure 2. Temporal variations in (a) absorption coefficients at 405 nm and start times of TEM sampling (A–D with arrows), (b) scattering coefficients at 405 nm, (c) absorption coefficients at 781 nm, (d) scattering coefficients at 781 nm, and (e, f and g) enhancement of light absorption (E_{abs}) at 405, 532 and 781 nm, respectively. Red, blue, and green symbols in (a–d) represent conditions of 25, 300 and 400 °C, respectively. Blue and green symbols in (e–g) represent E_{abs} [= $b_{abs}(\lambda, 25°C)/b_{abs}(\lambda, T)$] with T = 300 and 400 °C, respectively. The values are 3-h averaged data.

Figure 3. (a) Location of NOTOGRO in Ishikawa, Japan and (b-e) 72-hour backward air trajectories for air masses reaching the observation site at 500 m above sea level. These are colored with (b) b_{abs}(405 nm), (c) b_{abs}(781 nm), (d) E_{abs}(405 nm) and (e) E_{abs}(781 nm). The trajectories for E_{abs} calculated from b_{abs} data below the detection limit are represented as thin lines in (d) and (e).

Figure 4. The 72-hour horizontal backward trajectories for air masses reaching the observation site at 500 m above sea level during sampling periods A–D. Open dots along the trajectory represent the position of the air mass every 24 hour backward from the arrival point.

Figure 5. Number- (upper panels), cross-section area- and volume-based (lower panels) size distributions of aerosol particles during the sampling of samples A-D, as measured by SMPS. Red lines in the upper panels represent the number-based size distributions for particles measured without passage through the TD, while blue and green lines represent those for particles measured after passage through the TD maintained at 300 and 400 °C, respectively.

Figure 6. (a) Mass-based size distributions of rBC with log-normal best-fitting curves and (b) normalized-count distribution of lag time of the incandescent-light signal from the scattering signal for rBC with a mass equivalent diameter of 200 nm, obtained using the SP2 for samples A–D with best fit curves assuming the combination of two Gaussian functions. LT represents averaged lag-time.

Figure 7. Electron microphotographs before and after EDS analysis of samples (a, a') A and (b, b') D. Soot is shown by black triangles in (a') and (b'). Non-soot residues are shown by white triangles.

Figure 8. Morphological classification of particle types 1–7. Horizontal bars in the photographs represent a length of 0.5 μm. The pie chart in each morphological type represents the number fraction of compositional types classified based on the EDS analysis. The number below the pie chart represents the number of analyzed particles.

Figure 9. Classification of mixing states based on the comparison of electron micrographs for individual particles before (left) and after (right) irradiation by a high, densely electron beam: type *a*, non-volatile soot particles; type *b*, non-volatile particles except soot; type *c*, mixed particles of volatile material and non-volatile soot aggregate; type *d*, mixed particles of volatile material and non-volatile core without a soot-like shape; type *e*, semi-volatile particles; and type *f*, volatile particles. The pie chart in each mixing state type *a–f* represents the number fraction of compositional types determined by EDS analysis.

Figure 10. Size-segregated number proportions of (a) mixing state particle types on the basis of the classification in Figure 9, (b) morphological particle types on the basis of the classification in Figure 8 and (c) morphological particle types of soot-containing particles for samples A–D. The numbers above the columns show the number of particles observed.

Figure 11. Photographs of an aerosol sample after passage through the TD at 400°C sampled for 10 min from 09:38 May 6 (LT).

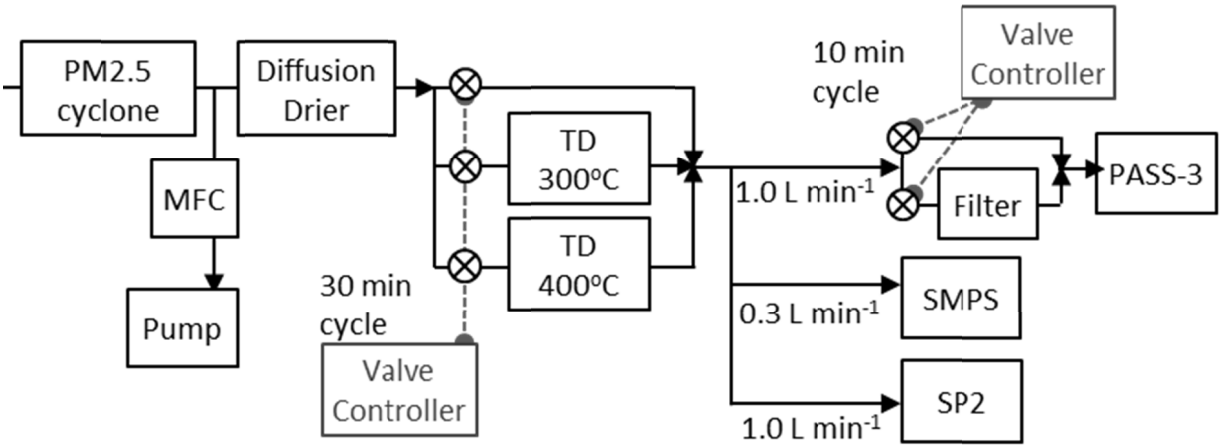

1

2

3 Figure 1.

4

5

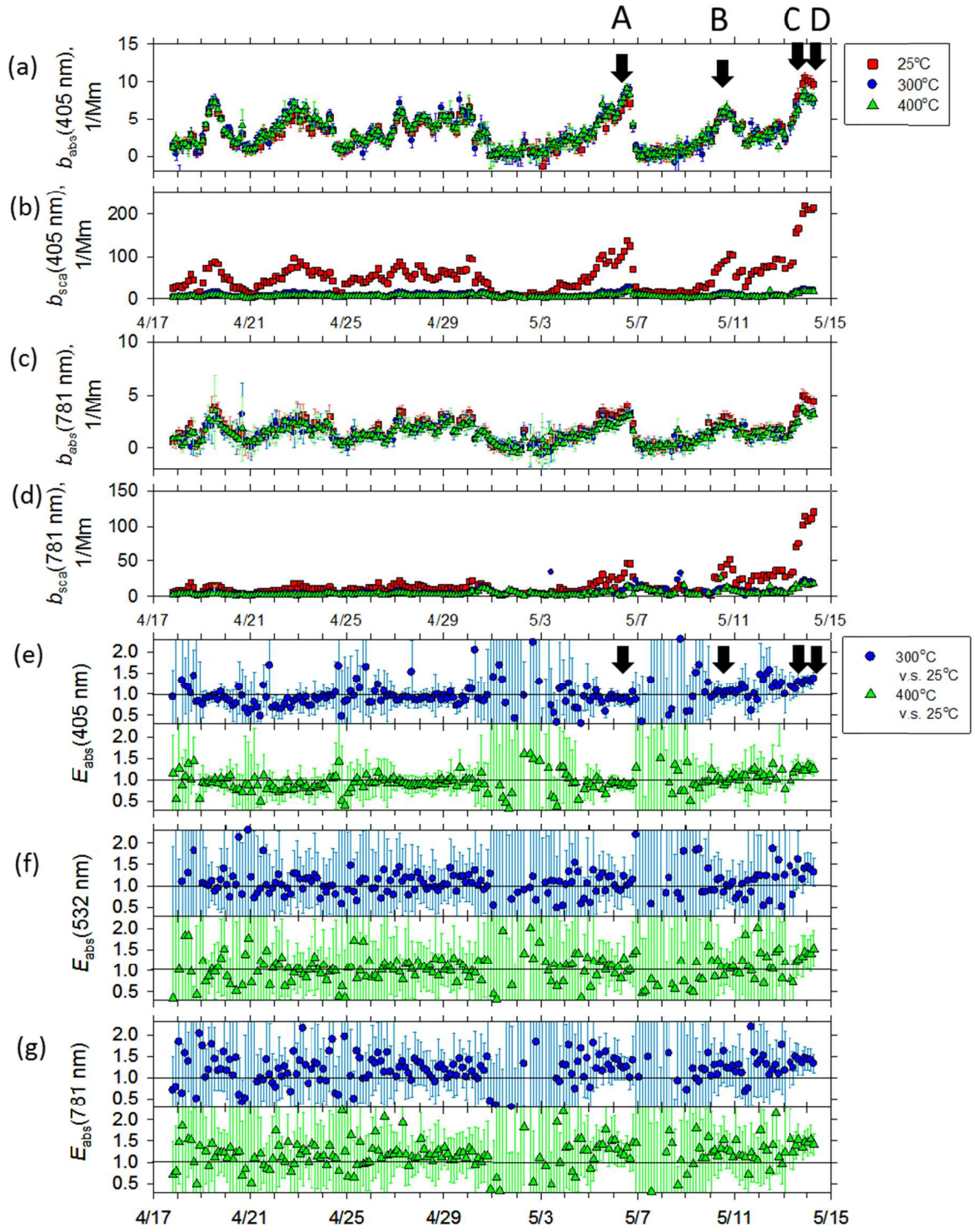
A
B
C D
(a)
b_{abs}(405 nm), 1/Mm
25°C
300°C
400°C
(b)
b_{sca}(405 nm), 1/Mm
(c)
b_{abs}(781 nm), 1/Mm
(d)
b_{sca}(781 nm), 1/Mm
4/17
4/21
4/25
4/29
5/3
5/7
5/11
5/15
(e)
E_{abs}(405 nm)
300°C v.s. 25°C
400°C v.s. 25°C
(f)
E_{abs}(532 nm)
(g)
E_{abs}(781 nm)

Figure 2.

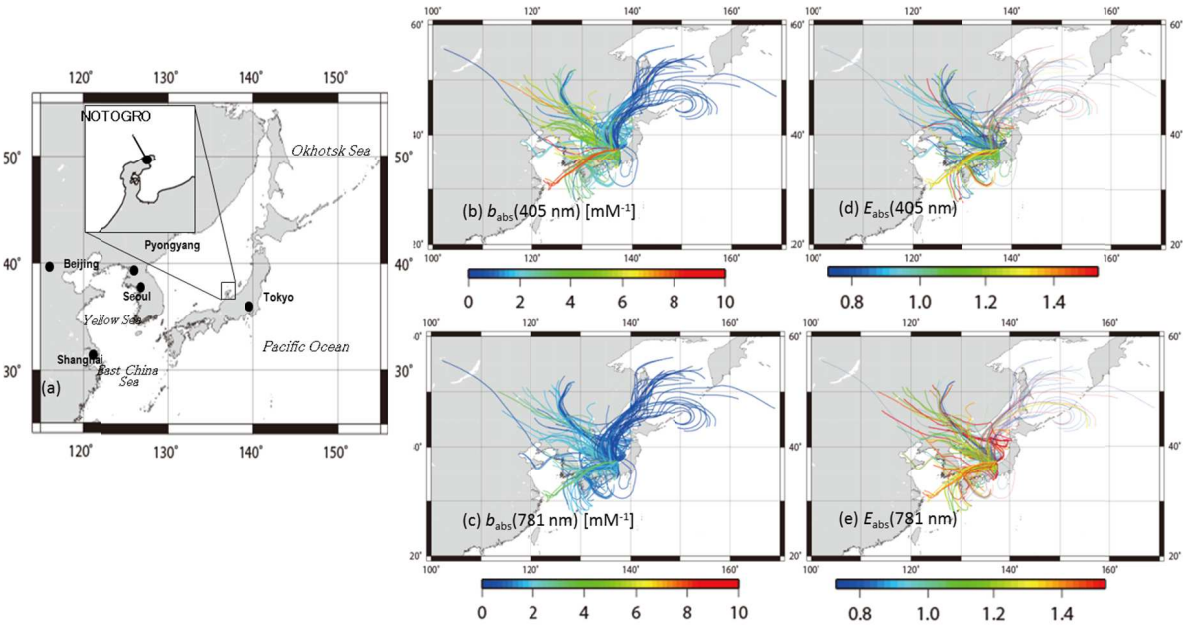

1

2

3 Figure 3.

4

5

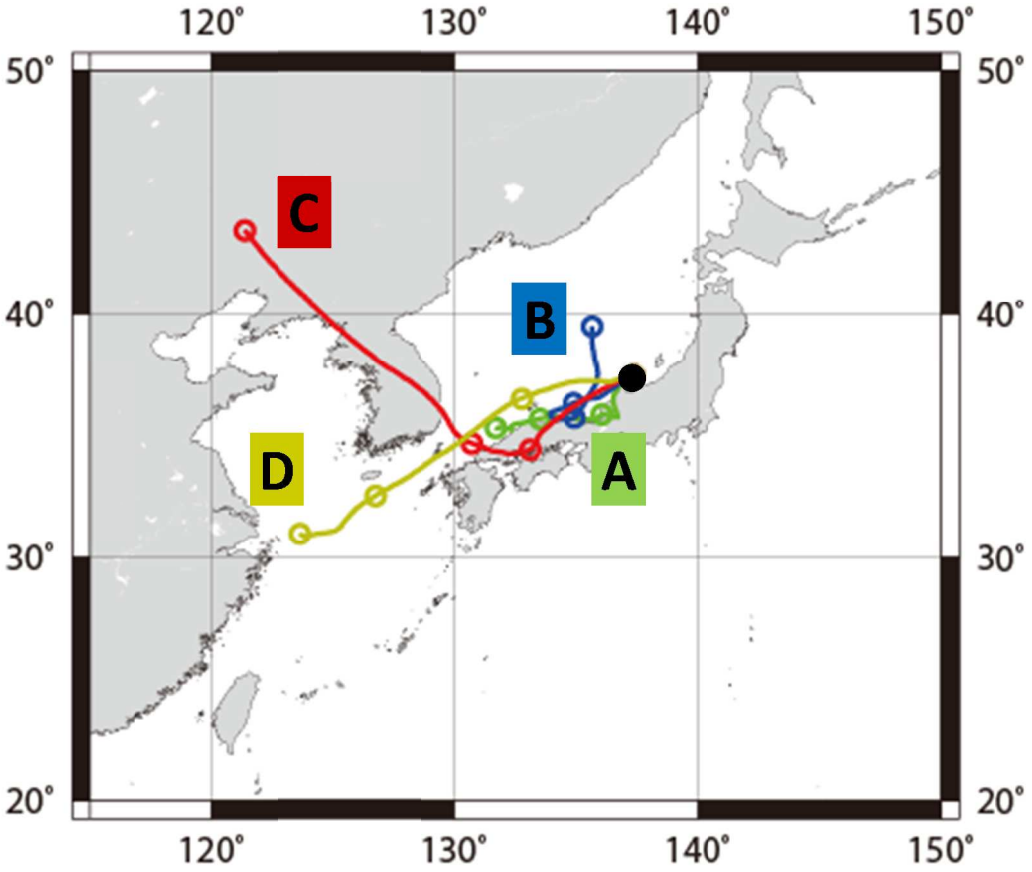

1

2 Figure 4.

3

1

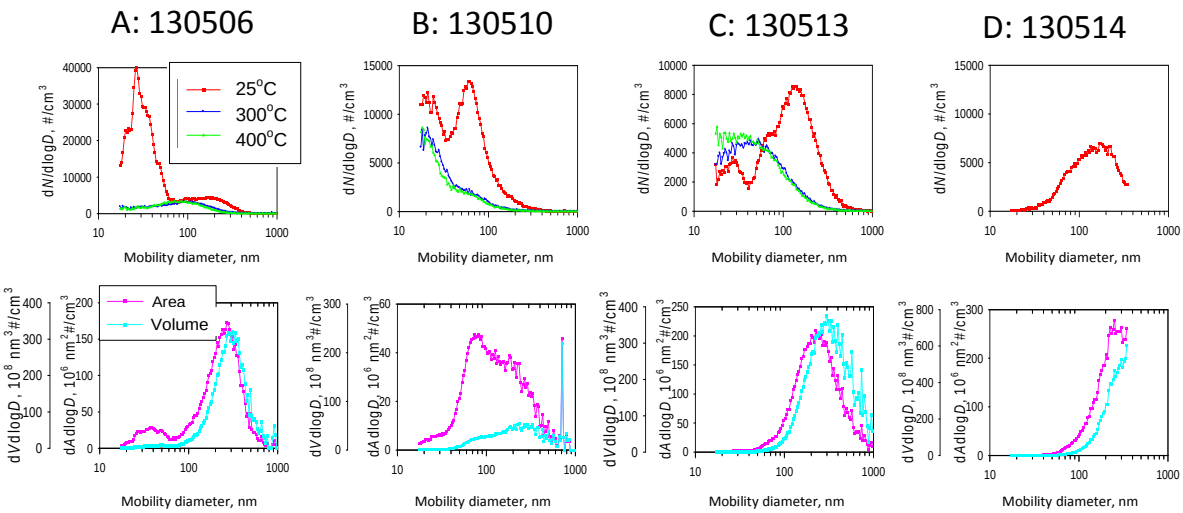

2

3 Figure 5.

4

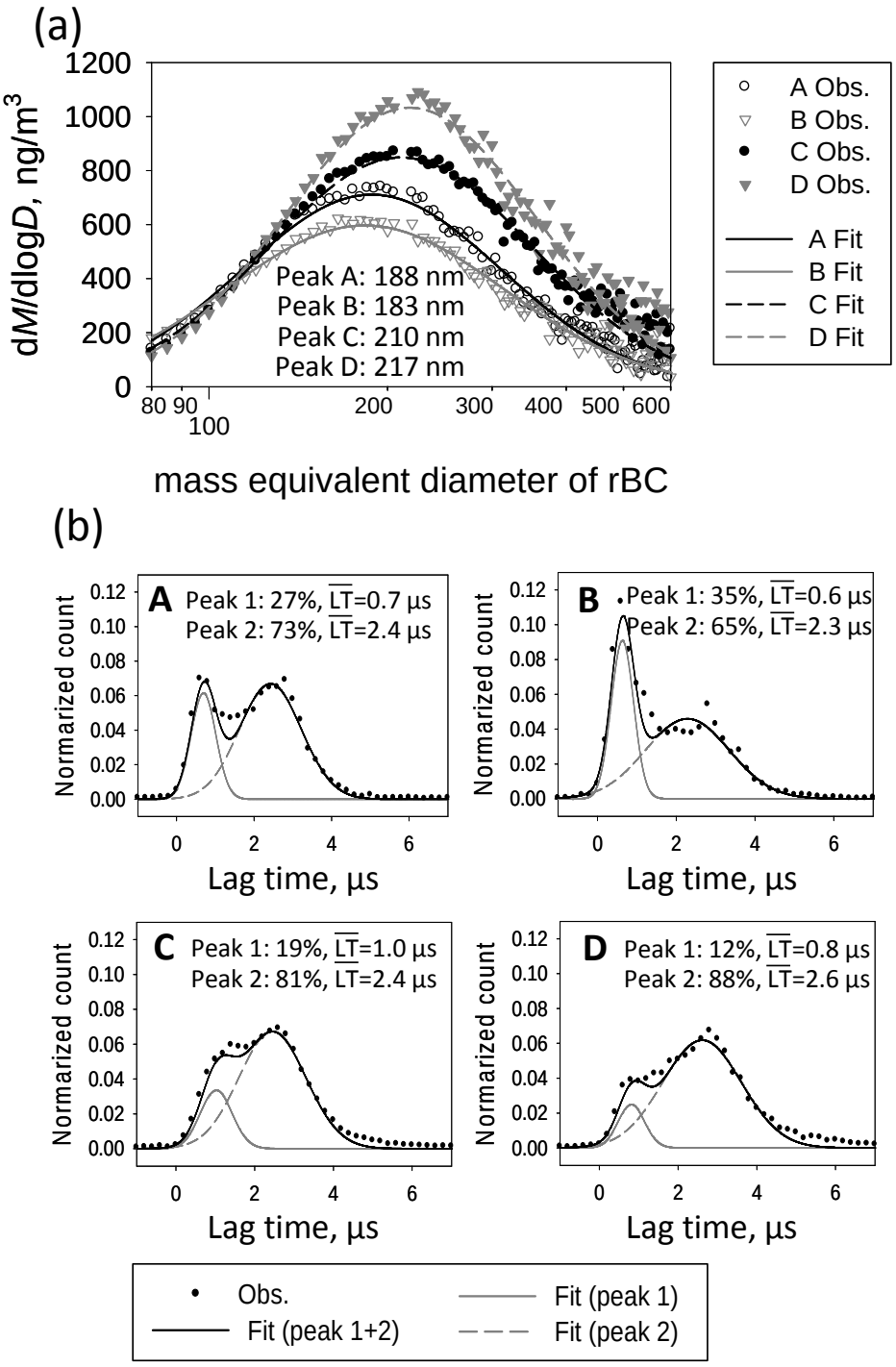
(a)
dM/dlogD, ng/m3
mass equivalent diameter of rBC
Peak A: 188 nm
Peak B: 183 nm
Peak C: 210 nm
Peak D: 217 nm
A Obs.
B Obs.
C Obs.
D Obs.
A Fit
B Fit
C Fit
D Fit
(b)
A Peak 1: 27%, LT=0.7 µs
Peak 2: 73%, LT=2.4 µs
B Peak 1: 35%, LT=0.6 µs
Peak 2: 65%, LT=2.3 µs
C Peak 1: 19%, LT=1.0 µs
Peak 2: 81%, LT=2.4 µs
D Peak 1: 12%, LT=0.8 µs
Peak 2: 88%, LT=2.6 µs
Normarized count
Lag time, µs
Obs.
Fit (peak 1+2)
Fit (peak 1)
Fit (peak 2)

Figure 6.

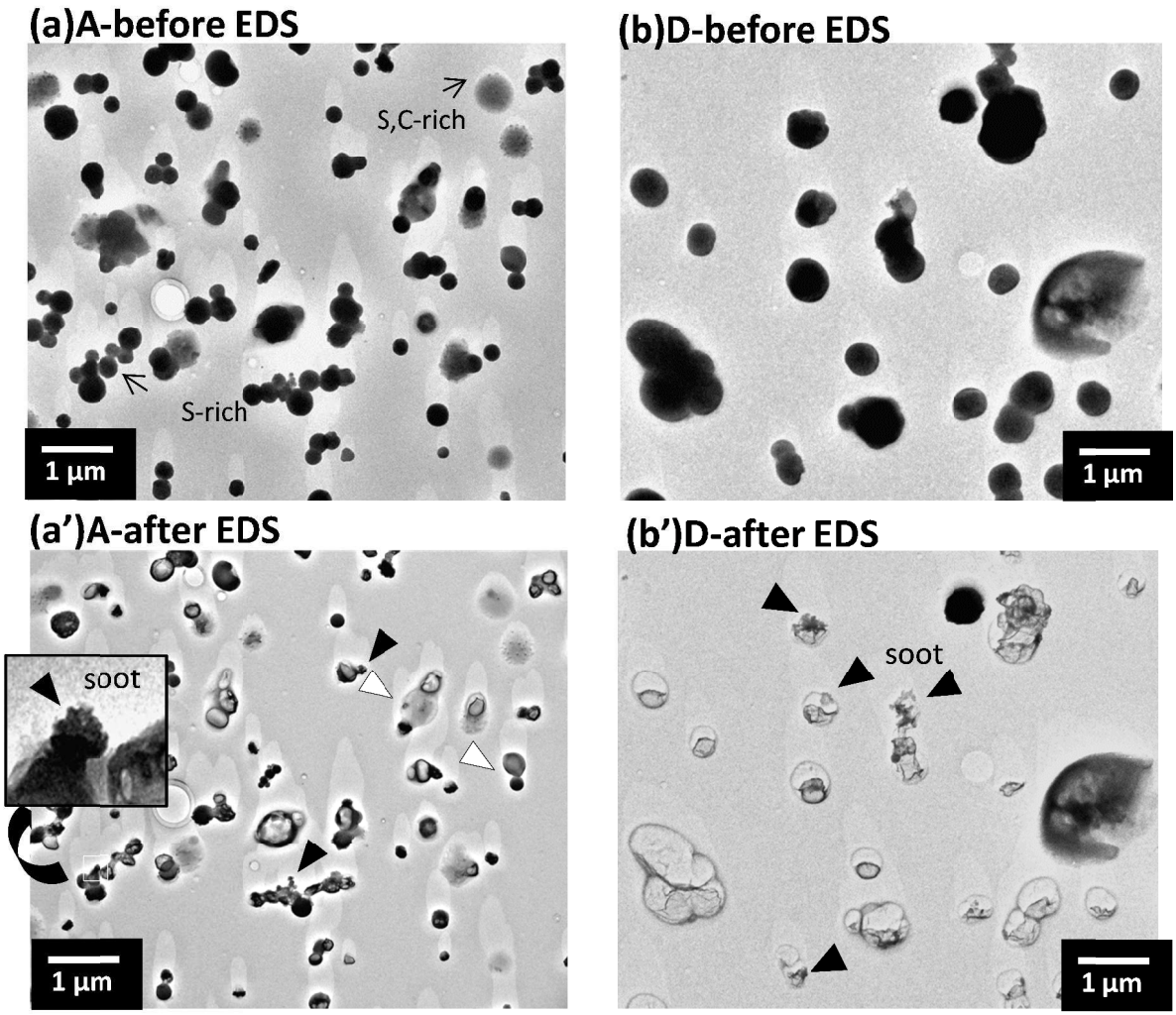
(a)A-before EDS
S,C-rich
S-rich
1 µm
(b)D-before EDS
1 µm
(a')A-after EDS
soot
1 µm
(b')D-after EDS
soot
1 µm

Figure 7.

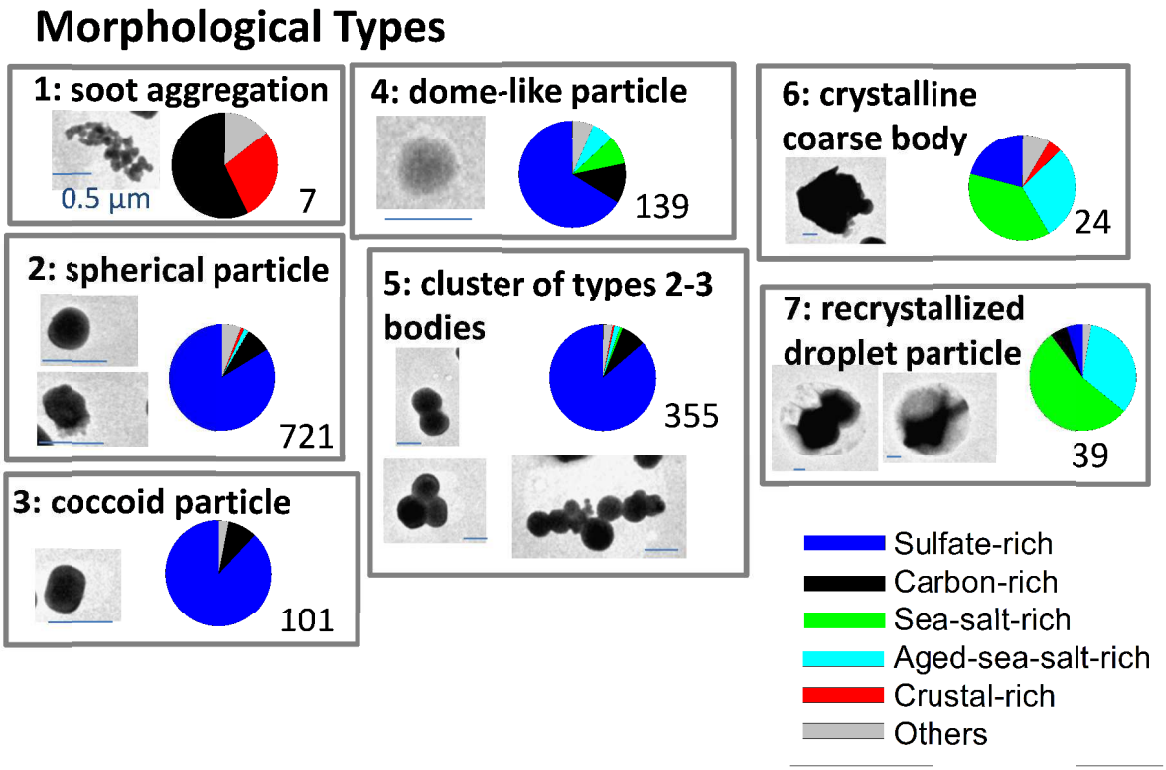
Morphological Types
1: soot aggregation
0.5 µm
7
4: dome-like particle
139
6: crystalline coarse body
24
2: spherical particle
721
5: cluster of types 2-3 bodies
355
7: recrystallized droplet particle
39
3: coccoid particle
101
Sulfate-rich
Carbon-rich
Sea-salt-rich
Aged-sea-salt-rich
Crustal-rich
Others

1

2 Figure 8.

3

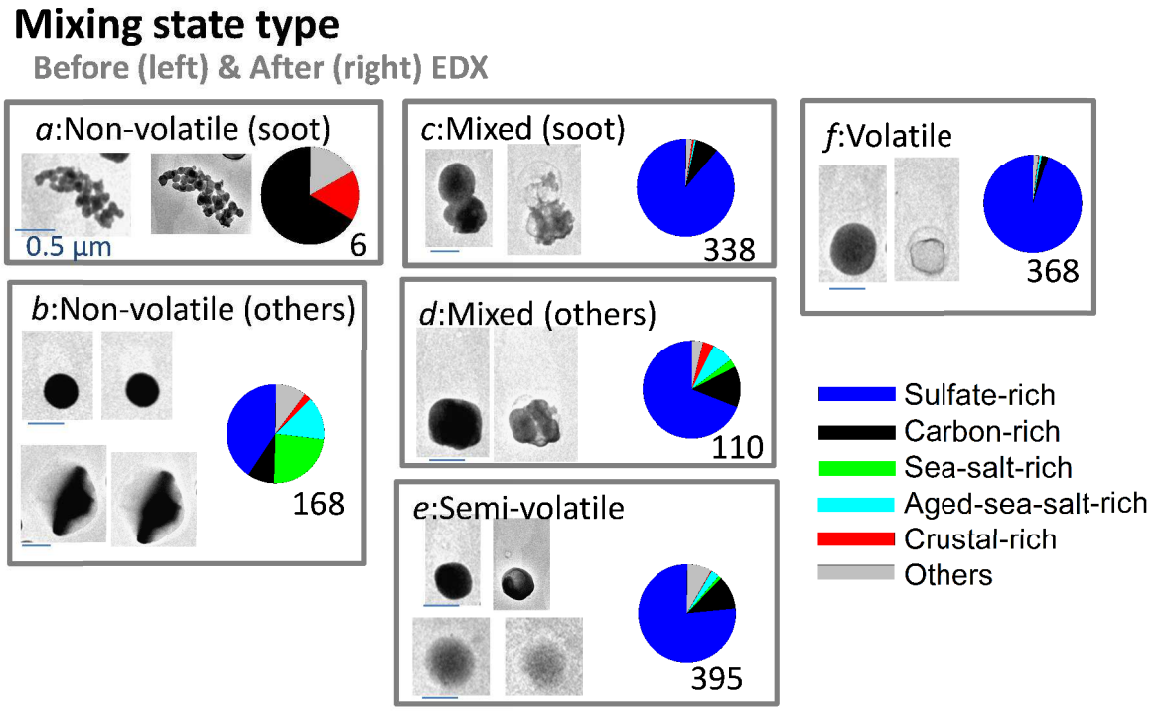

1

2

3 Figure 9.

4

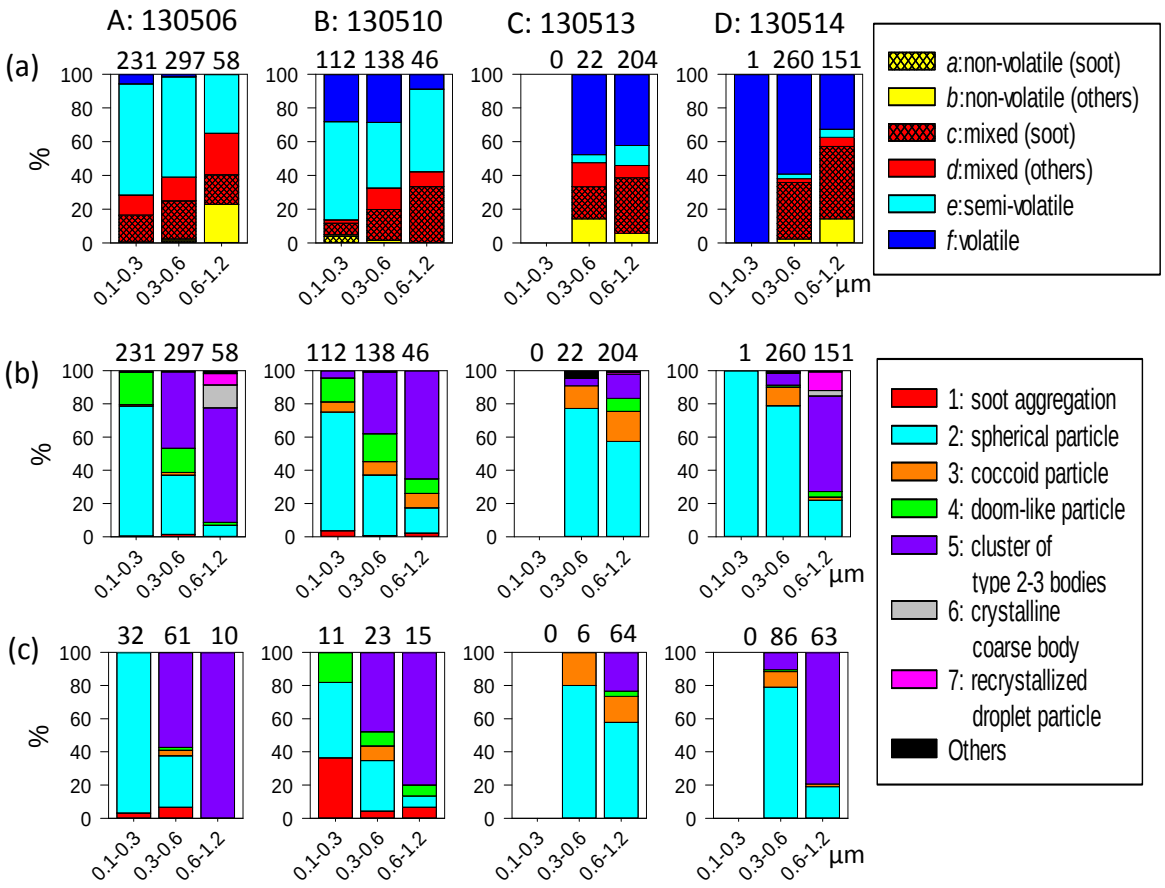
A: 130506
B: 130510
C: 130513
D: 130514
(a)
231 297 58
112 138 46
0 22 204
1 260 151
(b)
231 297 58
112 138 46
0 22 204
1 260 151
(c)
32 61 10
11 23 15
0 6 64
0 86 63
%
0.1-0.3
0.3-0.6
0.6-1.2
µm
a:non-volatile (soot)
b:non-volatile (others)
c:mixed (soot)
d:mixed (others)
e:semi-volatile
f:volatile
1: soot aggregation
2: spherical particle
3: coccoid particle
4: doom-like particle
5: cluster of type 2-3 bodies
6: crystalline coarse body
7: recrystallized droplet particle
Others

Figure 10.

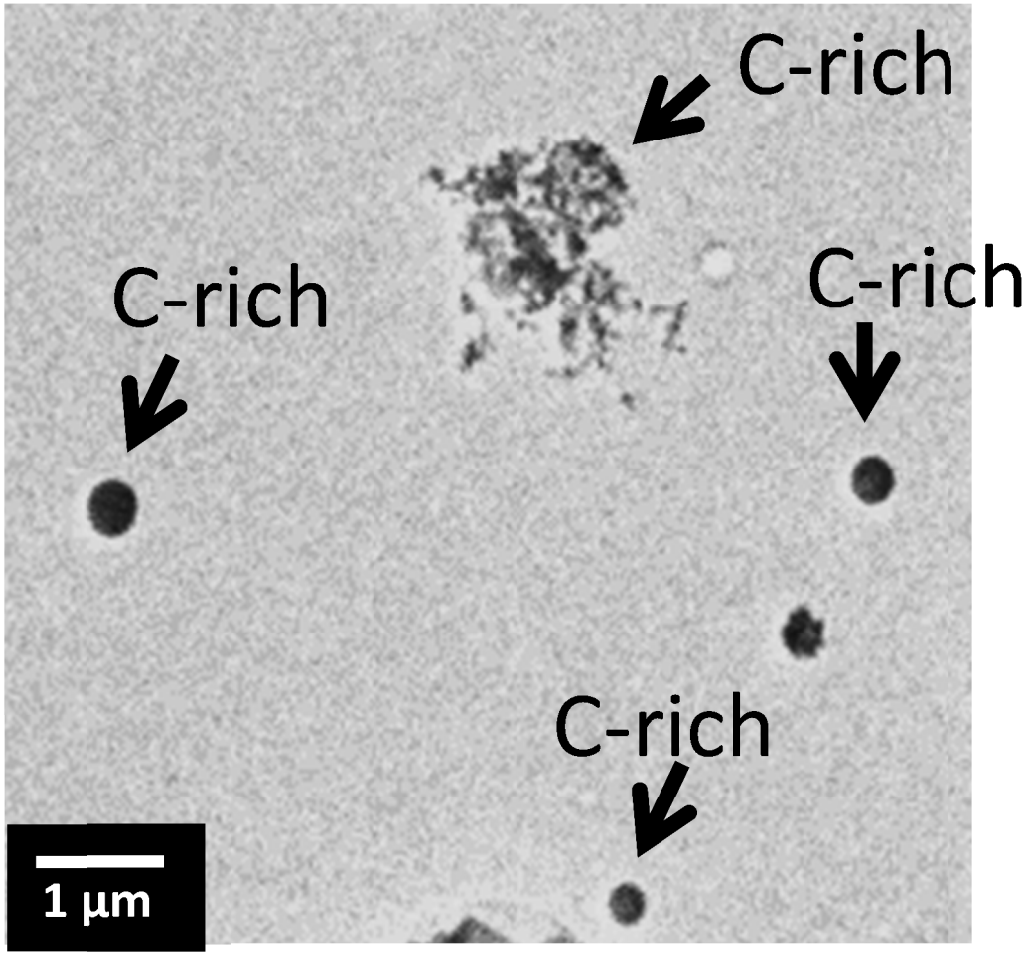

Figure 11.